Sentinel-1 backscatter analysis and radiative transfer modeling of dense winter wheat time series

Thomas Weiß, Thomas Ramsauer, Thomas Jagdhuber, Alexander Löw, Philip Marzahn

Angaben zur Veröffentlichung / Publication details:

Weiß, Thomas, Thomas Ramsauer, Thomas Jagdhuber, Alexander Löw, and Philip Marzahn. 2021. "Sentinel-1 backscatter analysis and radiative transfer modeling of dense winter wheat time series." *Remote Sensing* 13 (12): 2320. https://doi.org/10.3390/rs13122320.

remote sensing

MDPI

Article

Sentinel-1 Backscatter Analysis and Radiative Transfer Modeling of Dense Winter Wheat Time Series

Thomas Weiß [1,*], Thomas Ramsauer [1], Thomas Jagdhuber [2,3], Alexander Löw [1] and Philip Marzahn [1]

[1] Department of Geography, Ludwig-Maximilians-Universität München, Luisenstraße 37, 80333 Munich, Germany; t.ramsauer@iggf.geo.uni-muenchen.de (T.R.); alexander.loew@lmu.de (A.L.); p.marzahn@iggf.geo.uni-muenchen.de (P.M.)
[2] Microwaves and Radar Institute, German Aerospace Center, Münchener Straße 20, 92234 Wessling, Germany; Thomas.Jagdhuber@dlr.de
[3] Institute of Geography, University of Augsburg, Alter Postweg 118, 86159 Augsburg, Germany
* Correspondence: weiss.thomas@lmu.de

Abstract: This study evaluates a temporally dense VV-polarized Sentinel-1 C-band backscatter time series (revisit time of 1.5 days) for wheat fields near Munich (Germany). A dense time series consisting of images from different orbits (varying acquisition) is analyzed, and Radiative Transfer (RT)-based model combinations are adapted and evaluated with the use of radar backscatter. The model shortcomings are related to scattering mechanism changes throughout the growth period with the use of polarimetric decomposition. Furthermore, changes in the RT modeled backscatter results with spatial aggregation from the pixel to field scales are quantified and related to the sensitivity of the RT models, and their soil moisture output are quantified and related to changes in backscatter. Therefore, various (sub)sets of the dense Sentinel-1 time series are analyzed to relate and quantify the impact of the abovementioned points on the modeling results. The results indicate that the incidence angle is the main driver for backscatter differences between consecutive acquisitions with various recording scenarios. The influence of changing azimuth angles was found to be negligible. Further analyses of polarimetric entropy and scattering alpha angle using a dual polarimetric eigen-based decomposition show that scattering mechanisms change over time. The patterns analyzed in the entropy-alpha space indicate that scattering mechanism changes are mainly driven by the incidence angle and not by the azimuth angle. Besides the analysis of differences within the Sentinel-1 data, we analyze the capability of RT model approaches to capture the observed Sentinel-1 backscatter changes due to various acquisition geometries. For this, the surface models "Oh92" or "IEM_B" (Baghdadi's version of the Integral Equation Method) are coupled with the canopy model "SSRT" (Single Scattering Radiative Transfer). To resolve the shortcomings of the RT model setup in handling varying incidence angles and therefore the backscatter changes observed between consecutive time steps of a dense winter wheat time series, an empirical calibration parameter ($coef$) influencing the transmissivity (T) is introduced. The results show that shortcomings of simplified RT model architectures caused by handling time series consisting of images with varied incidence angles can be at least partially compensated by including a calibration coefficient to parameterize the modeled transmissivity for the varying incidence angle scenarios individually.

Keywords: soil moisture; radiative transfer models; winter wheat; Sentinel-1; time series

Citation: Weiß, T.; Ramsauer, T.; Jagdhuber, T.; Löw, A.; Marzahn, P. Sentinel-1 Backscatter Analysis and Radiative Transfer Modeling of Dense Winter Wheat Time Series. *Remote Sens.* **2021**, *13*, 2320. https://doi.org/10.3390/rs13122320

Academic Editors: Prasad S. Thenkabail, Jochem Verrelst, Clement Atzberger and François Waldner

Received: 3 March 2021
Accepted: 10 June 2021
Published: 13 June 2021

1. Introduction

The Sentinel-1 mission was designed for systematically mapping land surfaces with enhanced revisit frequency, coverage, timeliness, and reliability for applications and operational services requiring a long time series [1]. Two of these applications, using freely available Sentinel-1 data, are agricultural monitoring and modeling on regional or global scales [2,3]. The mission currently comprises a constellation of twin satellites, each with a revisit time of 12 days [4,5]. Thus, observations with the same acquisition geometry (exact

same orbit) are provided every six days. If multiple orbits (ascending and descending) and, therefore, various satellite acquisition geometries are considered, a revisit time of less than two days can be accomplished for most parts of Europe [6]. Furthermore, with the provision of space-borne radar data at such an unprecedented spatial and temporal resolution, research on crucial societal and economic challenges such as climate change [7,8] or food security [9–11] can be assessed. For future food security, the monitoring of winter wheat, as one of the most important cereals in Europe [12] and the crop type with the second-largest coverage worldwide, is considered fundamental [13]. One important environmental parameter for winter wheat growth is soil moisture, which shows high spatiotemporal variability [14,15]. Monitoring of the diurnal cycles of soil moisture and other natural fast changing processes with a dense time series [16] reveals possibilities for real-time management, such as of droughts or precision agriculture [17,18].

Lately, more and more studies using microwave time series data to estimate the soil moisture of agricultural areas—especially for the crop type winter wheat—have been conducted [19–21]. Often, only a single satellite orbit constellation and, therefore, data from one satellite with the same acquisition geometry are used [19,22–24]. Occasionally, the time series used consists of data from the same satellite but related to different orbits and, thus, various azimuth or/and incidence angles [20,23,25–27]. Only a few of these studies also use data from different sensors to retrieve soil moisture values [23,27,28]. Summarizing the above studies, one established approach is to simulate radar backscatter or to estimate soil moisture of vegetated areas by using radar backscattering models based on the Radiative Transfer (RT) equation [29,30]. These model simulations of radar backscatter from agricultural fields are based on sensor and platform configurations (e.g., incidence angle, azimuth angle, frequency, and polarization), soil properties (e.g., soil moisture, texture, and surface roughness), and vegetation parameters (e.g., Leaf Area Index (LAI), Normalized Difference Vegetation Index (NDVI), Vegetation Water Content (VWC), and biomass) [19,29]. In recent decades, several complex models such as the Michigan Canopy Scattering Model (MIMICS) [31], the Tor Vergata model [32], a first-order radiative transfer model from Quast [33,34], and a Wheat Canopy Scattering Model (WCSM) [27] have been developed for modeling the electromagnetic scattering of different vegetation types by using the first or second order of the RT equation. For precisely modeling the backscatter characteristics that occur during different phenology stages of winter wheat, complex models with detailed information, such as their canopy element size and distribution (length; diameter; thickness; and water content fraction of the stem, leaf, and ears) are needed to account for a multi-layer volume canopy [27]. Thus, different electromagnetic scattering interactions, for example, direct canopy scattering and single or multiple interactions between canopy parts (the ear, leaf, and stem) and the surface, can be modeled. A problem with using these complex models is the provision of additional input data for characterization of the canopy. Therefore, canopy models with fewer input parameters such as the empirical WCM [35], in which only the direct volume backscatter part is considered; a modified version of WCM (MWCM) [36]; or a Single Scattering Radiative Transfer (SSRT) model described by Ulaby [30] or De Roo [37], in which various scattering mechanisms are modeled in a simpler way, are regularly used [26,30,37–40]. Additionally, information about the surface scattering contribution under winter wheat fields for the estimation of soil moisture is crucial. Commonly used surface backscattering models are the surface scattering part of the empirical Water Cloud Model (WCM) [35]; the semi-empirical models of Oh (Oh92, Oh04) [41,42] and Dubois [43]; and physical models, such as the Integral Equation Method (IEM) [44] in its original form or as adapted by Baghdadi (IEM_B) [45].

In the scope of using dense microwave time series for monitoring winter wheat fields around the world, complex model approaches might not be applicable most of the time due to the lack of detailed in situ measurements on soil and winter wheat characteristics. Model approaches with a low number of required input parameters that can be provided by satellite remote sensing (e.g., LAI) are preferred when applied on the global scale. Therefore, in this study, we investigate how a simplified RT model for the canopy part

(SSRT) in combination with two surface backscattering models (Oh92 and IEM_B) are able to simulate backscattering for a dense time series with various acquisition geometries and how far the RT model can be adapted by means of an empirical parameter to compensate for the lack of detailed in situ wheat canopy information. The simple RT models used in their original form are not completely optimized for wheat scattering, and a separation of contributions from vegetation growth and geometric configuration is a challenging task. Thus, the main focus is set on how changes in acquisition geometries (changes in azimuth and incidence angles) affect the simplified backscattering models throughout the entire wheat growing period and if an empirical parameter is able to compensate for these effects up to a certain extent. The contributions from vegetation growth and the geometric configuration difference in the multi-temporal signature are separated.

By investigating a dense Sentinel-1 time series of winter wheat fields in southern Germany, the following questions are answered within this paper:

(A) Do backscatter variations between individual Sentinel-1 scenes with various acquisition geometries depend on changes in incidence and/or azimuth angle?
(B) How do backscatter calculations of simple RT model approaches react to changes in terms of acquisition geometry, and what are the probable scattering mechanism variations for winter wheat fields?
(C) What influence (in dB) do different spatial backscatter aggregation scenarios have on RT model results?
(D) How do uncertainties in backscatter (variation by 0.2 dB, 0.5 dB, and 1.0 dB) influence soil moisture estimations in the RT models analyzed during the vegetation growing period of winter wheat?
(E) How should one best assess scattering from wheat fields in terms of acquisition scenario, preprocessing, and soil moisture estimation using time series information?

2. Data Sets

2.1. Study Area

In situ measurements obtained from the Munich North Isar (MNI) test site in 2017 were used for this study. The study area (48°13′N–48°20′N, 11°39′E–11°45′E, Figure 1) is located to the north of Munich, Bavaria, southern Germany. The test site was established in 2014, and since then, almost every year during the vegetation period, in situ campaigns are carried out to survey the agriculturally relevant key variables [26,46–49]. The main crop types within the MNI test site were wheat, maize, and grassland. The meteorological measurements were provided by three meteorological stations: in Freising, in Eichenried, and at the Munich airport. All three stations are situated within a 10 km radius around the MNI test site. The permanently installed facilities in Freising (470 m a.s.l.) and Eichenried (475 m a.s.l.) are operated by the Bavarian State Research Center for Agriculture (LFL). The meteorological station at the Munich airport (446 m a.s.l.) is operated by the German Meteorological Service (DWD). The meteorological station records reported an annual mean temperature of 9 °C (Freising) to 9.3 °C (Eichenried) and an average annual precipitation of 753 mm (Munich-airport) to 853 mm (Eichenried) for the year 2017. The region around the test site exhibits only marginal changes in height (above sea level) and has no significant topographic variation.

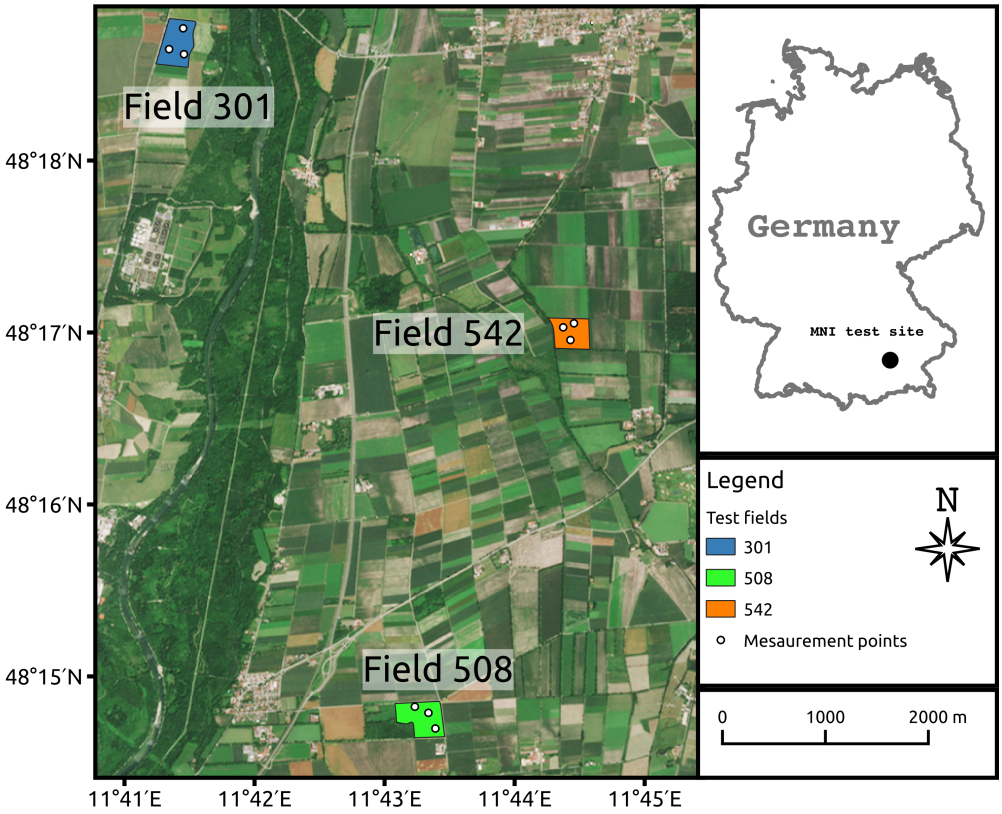

Figure 1. Overview of the study area Munich-North-Isar (MNI) with test fields 508 (green), 542 (orange), and 301 (blue), each with three sampling points.

2.2. Field Data

Between March and July 2017, in situ measurements of soil and vegetation parameters of wheat fields for the validation of retrieval schemes based on different satellite sensors, such as Sentinel-1, Sentinel-2, or Environmental Mapping and Analysis Program (EnMAP), were conducted (Table 1). For each field under investigation, three sample points were chosen (Figure 1). At each location, weekly vegetation height and LAI measurements as well as assessments of plant phenology (based on BBCH-scale) were taken. For total LAI measurements, the average of 14 samples from the same area measured with a LI-COR Biosciences LAI-2200C device (LI-COR Biosciences Inc., Lincoln, NE, USA) was used. The LAI measurements reach a calculated accuracy of 0.45 m^2/m^2 to 0.52 m^2/m^2 in terms of the mean standard deviation of repeated measurements within fields. Soil moisture was monitored using permanently installed Decagon TM5 sensors (Decagon Devices Inc., Pullman, WA, USA). The soil moisture devices were installed within the first five centimeters of the soil surface with a monitoring time interval of 10 min. Laboratory analysis of the soil texture of previous field campaigns reports no evidence of significant micro-locational soil variations within the test site [48]. The soil properties presented in Table 2 show values for soil bulk density, 1.45 $\pm$ 0.13 g/cm^3; for clay content, 7.38 $\pm$ 1.8%; for silt content, 68.55 $\pm$ 11.64%; and for sand content, 24.08 $\pm$ 10.46%.

Table 1. Acquisition time, time interval, and range of dynamic in situ measurements.

Variable	Acquisition Time	Time Interval	Range
Canopy height [cm]	24 March–17 July 2017	weekly	7–105
LAI	24 March–17 July 2017	weekly	0.35–6.25
Soil moisture [m^3/m^3]	24 March–17 July 2017	every 10 min	0.09–0.38

Table 2. Laboratory results for sand, clay, and bulk content of the soil surface samples.

Variable	Time Interval	Mean	Std
Soil sand content [%]	once (several locations)	24.08	10.46
Soil silt content [%]	once (several locations)	68.55	11.64
Soil clay content [%]	once (several locations)	7.38	1.80
Bulk density [g/cm^3]	once (several locations)	1.45	0.13

2.3. Satellite Data

A dense time series of Sentinel-1 A/B (C-band, Level-1 SLC) satellite data was used for this study. Preprocessing of the SAR data was accomplished by using ESA's SNAP Toolbox Version 7.0.3. SRTM data with 1 arc-second spatial resolution were used as a digital elevation model for geometric correction of the SAR data [50,51]. For radiometric correction, the method of Kellndorfer et al. [52] was applied. To reduce the impact of speckle by simultaneously maintaining the spatial resolution, a multi-temporal Lee-sigma filter was chosen. For each Sentinel-1 acquisition, information from six other acquisitions (three before and three after the target) was used for temporal filtering. A spatial window of 5 × 5 pixels, sigma of 0.9, and a target window size of 3 × 3 served as the Lee filter parameters. For the images used during temporal filtering, no separation with respect to different orbits was performed. A comparison of the temporal filtered data—using images from different orbits versus using images from the same orbit—shows almost no difference between the filtered output data. After all of the preprocessing steps, the data were resampled to a spatial resolution of 10 × 10 m [26]. In 2017, the MNI test site area was covered by four different Sentinel-1 tracks with individual acquisition geometries regarding incidence angle, azimuth angle, and orbit direction. Considering all available Sentinel-1 images for 2017 at the MNI test site, a revisit time of 1.5 days was reached. A total of 78 Sentinel-1 scenes during the time of the field campaign are available. For our study, the focus was set to VV polarization, motivated by previous findings where, to retrieve soil moisture, the usage of VH polarization alone or in addition to VV polarization was not suitable for well-developed agricultural vegetation [23,53]. Table 3 summarizes the Sentinel-1 data set used and its respective image properties.

Table 3. Available Sentinel-1A/B satellite data for the MNI field campaign period in 2017 (23 Match–17 July 2017).

Orbit		Mean Incidence Angle	Azimuth Angle	Acquisition	Amount	Revisit Time
Mode	Rel. Nr.	of Test Site Area [°]	Relative to North [°]	Time		[Days]
Asc	44	36	−15	4:58 p.m.	19	6
	117	45	−15	5:06 p.m.	19	6
Des	95	43	−165	5:17 a.m.	20	6
	168	35	−165	5:25 a.m.	20	6

3. Method

Our study focused on investigating a dense Sentinel-1 C-band backscatter time series under varying acquisition geometries and on RT-based backscatter modeling of the time series. Two different RT model combinations calculating VV-polarized backscatter were analyzed. The soil surface scattering models used were Oh92 [41] and Baghdadi's version of the IEM [45], hereafter referred to as IEM_B. The surface models were coupled with the Single Scattering Radiative Transfer Model (SSRT) of [30,37]. The SSRT was chosen because it calculates the direct vegetation volume backscatter and backscatter contributions due to the surface–canopy interactions. The calibration approach of Weiß et al. [26] with a non-static empirical parameter ($coef$) influencing the one-way transmissivity of the canopy (T) was used. Therefore, only one empirical parameter was calibrated for the different model combinations. The approximations applied by Weiß et al. [26] for parameters with missing in situ data such as rms height (1.2 cm) or scattering albedo (0.03) were used. The other input parameters for the surface models were in situ data for soil properties such

as clay and sand content, bulk density, and soil moisture measurements. For the canopy model part, in situ data of canopy height and LAI were used as vegetation descriptors. The various scattering components (ground component $\sigma^0_{g_{pq}}$, canopy component $\sigma^0_{c_{pq}}$, total canopy ground contribution $\sigma^0_{cgt_{pq}}$, and ground canopy ground contribution $\sigma^0_{gcg_{pq}}$) of the SSRT used by De Roo et al. [37] and Ulaby [30] are defined as

$$\sigma^0_{pq} = \sigma^0_{g_{pq}} + \sigma^0_{c_{pq}} + \sigma^0_{cgt_{pq}} + \sigma^0_{gcg_{pq}}, \tag{1}$$

with

$$\sigma^0_{g_{pq}} = T_p T_q \, \sigma^0_{s_{pq}}, \tag{2}$$

$$\sigma^0_{c_{pq}} = \frac{\sigma^{back}_{V_{pq}} \, cos\theta}{k^p_e + k^q_e} \, (1 - T_p T_q), \tag{3}$$

$$\sigma^0_{cgt_{pq}} = \sigma^{bist}_{V_{pq}} \, H \, [R_p + R_q] \, T_p T_q \quad \text{and} \tag{4}$$

$$\sigma^0_{gcg_{pq}} = \frac{\sigma^{back}_{V_{pq}} \, cos\theta}{k^p_e + k^q_e} \, (R_p R_q - T_p T_q). \tag{5}$$

where $\sigma^0_{s_{pq}}$ represents the surface scattering, T_p and T_q symbolize the transmissivity of the canopy, $\sigma^{back}_{V_{pq}}$ is the volume backscattering coefficient of the vegetation medium, $\sigma^{bist}_{V_{pq}}$ is the bi-static scattering cross section, θ is the incidence angle, k_e is the extinction coefficient for the different polarizations, H is the canopy height, and R describes the Fresnel reflectivity by polarization pq. T is defined as

$$T_p = e^{-k^p_e \, H \, sec\theta}. \tag{6}$$

To calibrate the transmissivity of the canopy (T) for different time steps and various acquisition scenarios, the extinction coefficient k_e for polarization p and q is defined as

$$k^p_e = coef * \sqrt{LAI}, \tag{7}$$

with LAI as the vegetation descriptor and $coef$ as the calibration coefficient. A more detailed overview of the different RT models is provided in Weiß et al. [26]. A summary of validity ranges, model types, and input parameters required for the applied models is listed in Table 4.

Table 4. Overview of the different surface models Oh92 and IEM_B as well as the canopy model SSRT in terms of type, validity range, required input parameters, and polarization. Separation of the input parameter applied for the RT models in calibrated parameters and in parameters from field measurements or literature values.

	Type	Validity Range	Required Parameters		Polarization
			Calibrated	Field Measurements or Literature Values	
Oh92	semi-empi.	$10° < \theta < 70°$ $0.1 < ks < 6$ $9 < mv < 31$ Vol.%		s, k, θ, ϵ $(clay, sand, bulk, mv)$	HH, VV VH
IEM_B	semi-empi.	$10° < \theta < 70°$ $ks \leq 3$		$s, k, l, \theta, \epsilon$ $(clay, sand, bulk, mv)$	HH, VV VH
SSRT	semi-empi.		ke $(coef)$	H, LAI, θ, ω	HH, VV VH

3.1. Calibration and Analyzed Data Sets

Figure 2 schematically explains the calibration approach from Weiß et al. [26] that was applied. Depending on the analysis approach, the images of the dense Sentinel-1 time series were separated into different subsets (blue box in Figure 2). An overview of the

data subsets used is provided in Table 5. Additionally, variations due to diverse spatial aggregation scenarios of the Sentinel-1 backscatter were investigated. An overview of the analyzed aggregation scenarios is given in Table 6. For each (sub)set and each aggregation scenario, the empirical parameter $coef$ is calibrated separately. Therefore, the sum of the squared difference between the modeled and measured VV-polarized backscatters were used as a minimization function to calibrate the parameter $coef$ and thus the transmissivity T (see Equations (6) and (7)). In the end, a final time series for $coef$ and thus a final RT modeled VV polarized radar backscatter time series was obtained.

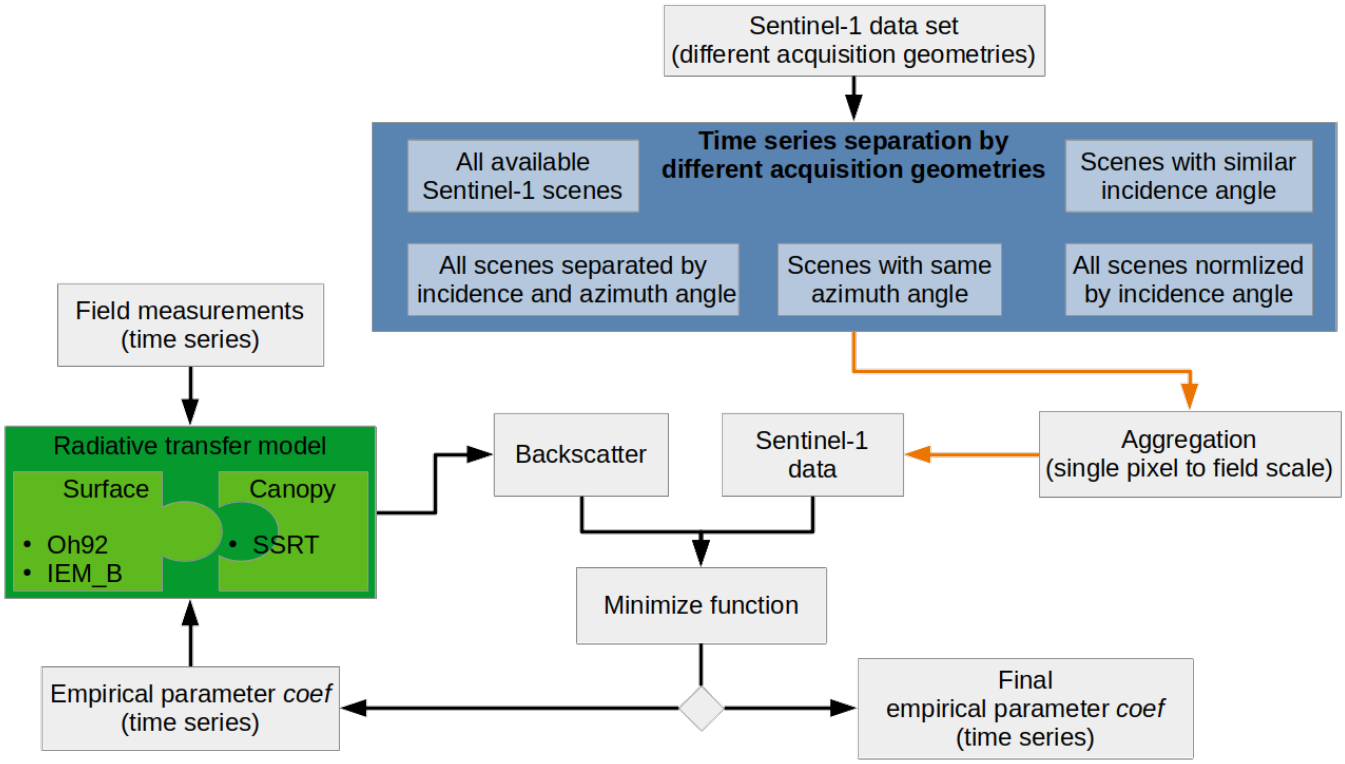

Figure 2. Schematic illustration of the calibration approach. Green box show used RT model combinations. The blue box illustrates the various (sub)sets analyzed for the dense time series. The orange arrows symbolize that several data (sub)sets and spatial aggregation scenarios were used.

Table 5. Investigated time series (sub)sets.

Abbreviation	Data Sets	Amount of Scenes	Rel. Orbit
All	All available Sentinel-1 scenes	78	44 + 95 + 117 + 168
Inci	Sentinel-1 scenes with similar incidence angle but different azimuth angle	2 sets of 39	44 + 168; 95 + 117
Azi	Sentinel-1 scenes with same orbit mode and zimuth angle	2 sets of 39	44 + 117; 95 + 168
Sep	Sentinel-1 scenes separated by incidence and azimuth angle	4 sets of 19–20	44; 95; 117; 168
Norm	All available Sentinel-1 scenes normalized to an incidence angle of 35°	78	44 + 95 + 117 + 168

Table 6. The backscatter aggregations investigated.

Abbreviation	Backscatter Aggregation	Area Size	Amount of Pixel
SP	Single pixel	10 × 10 m	1
30 m	15 m buffer	30 × 30 m	9
50 m	25 m buffer	50 × 50 m	25
100 m	50 m buffer	100 × 100 m	100
FS	Field scale		724–963

3.2. Leave-One-Out-Cross-Validation of Calibrated Model Combinations

A leave-one-out cross-validation approach was chosen to validate the calibrated model results of the different measurement points. Thus, the mean of eight out of nine measurement points of calibrated parameter $coef$ was validated with the remaining one. Since the model input parameters used show multi-dimensional and unstructured inter- and intra-field correlations, independence between the different measurement points was assumed [26]. To evaluate the RT model fit of the time series sets analyzed (Table 5), the unbiased Root Mean Square Error (ubRMSE) [54] as a statistical metric was used. The ubRMSE is calculated as follows

$$\text{ubRMSE} = \sqrt{\frac{1}{N}\sum_{i=1}^{N}[(x_i - \overline{x}) - (y_i - \overline{y})]^2} \quad (8)$$

where x represents the backscatter modeled, $\overline{x}$ represents the backscatter modeled and averaged, y represents the Sentinel-1 backscatter observation, $\overline{y}$ represents the averaged Sentinel-1 backscatter observation, i represents a specific sample, and N represents the total number of samples.

3.3. Sensitivity Analysis of Soil Moisture and Polarimetric Eigen-Based Decomposition for the RT Model

A sensitivity analysis of the RT models was conducted for a comprehensive interpretation of improvements in terms of backscatter values by using different Sentinel-1 time series sets (Table 5) and/or various spatial aggregations (Table 6). To test the RT models' sensitivity to changes in soil moisture, artificial deviations in soil moisture were assumed, leading to changes in backscatter values of 0.2 db, 0.5 db, or 1.0 dB. The artificial deviations in backscatter were calculated for each time step of the time series individually. In this way, the sensitivity of the backscatter to soil moisture during the phenological cycle and different meteorological conditions could be assessed.

In addition, a dual-polarized (VV and VH) eigen-based (entropy (H)-scattering alpha (alpha)) decomposition of the entire Sentinel-1 time series, having variations in the acquisition scenario, was performed to investigate and understand the occurring scattering mechanisms and changes in scattering mechanisms during the growing season. The H-alpha dual polarized decomposition [55] was performed by using an internal processing step of ESA's SNAP toolbox. Special focus was set on the comparison of images of consecutive time steps with various acquisition geometries. The dual-polarimetric eigen-based decomposition comes with a caveat, as the separation of different scattering mechanisms in the H-alpha plane is only possible with fully, quad-, or co- (VV and HH) polarized data [56]. Therefore, the exact identification and detailed distinction of the scattering mechanism that occurs for each time step is beyond the scope of information from the recorded data set. Nevertheless, the H-alpha results can be used as a first-order indicator of scattering mechanism change over time and, owing to acquisition scenario, even if the exact types of scattering mechanisms and their change cannot be identified directly. However, the scattering mechanism changes that were revealed might further improve our understanding of the deficits of simplified model approaches and how they might be compensated.

4. Results

4.1. All Sentinel-1 Tracks Analyzed as One Time Series

The calibration results analyzing the usage of different dense time series (sub)sets are presented for field point 508-1 as an example. The other fields analyzed and the respective intra-field points show similar patterns and are only included for validation of the backscattering model results (Section 4.3). Accordingly, a time series of VV-polarized backscatter of all available Sentinel-1 images for field point 508-1 (black line) is illustrated in Figure 3a. The model results (green and blue line) are based on a calibration of the empirical parameter $coef$ (Equation (7)) as part of the transmissivity (Equation (6)) considering all available Sentinel-1 images as one data set (Tables 5 and 6, "All-50 m"). The background colors red, blue, green, and yellow symbolize the Sentinel-1 data, and the respective acquisition geometries represent four consecutive days of Sentinel-1 data acquisition. A closer look at the four consecutive time steps (yellow to green background colors), while disregarding backscatter changes due to soil moisture and vegetation dynamics, shows that, during early vegetation stages (tillering and stem elongation), higher Sentinel-1 backscatter values are observed for more steep incidence angles (around 35°) than for more shallow ones (around 44°). Starting from the beginning of June (phenology stage booting), the backscatter behavior pattern in terms of the incidence angle variation of the four consecutive time steps varied. Accordingly, higher backscatter values were observed for incidence angles of 44° than for 35°. A pattern regarding variations in azimuth angles was not observed here. Comparing the modeled results of IEM_B with SSRT (green line) and of Oh92 with SSRT (blue line), higher sensitivities to incidence angle deviations are observed for the Oh92 model. Backscatter modeling for the phenology stages tillering and stem elongation of model Oh92 with SSRT reveals a high correlation with the Sentinel-1 backscatter observed in terms of absolute values and the changes in backscatter observed due to the various acquisition geometries. Starting from phenology stage booting to senescence, Sentinel-1 backscatter reveals a different behavior from the modeled results. For these phenology stages, the Sentinel-1 backscatter values of consecutive time steps with varying incidence angles (background colors yellow to red) increased whereas the RT model results exhibited a decrease in backscatter. For the other consecutive time steps with varying incidence angles (background colors blue to green), the Sentinel-1 backscatter values decreased whereas the RT model results showed an increase in backscatter. The different results of the Sentinel-1 and RT models are hereinafter referred to as a trend mismatch of consecutive time steps. Summarizing the findings, the simple RT model approaches experience difficulties in accurately modeling time series comprising observations from different orbits (different observation geometries) for a winter wheat field with a fully developed canopy. A trend mismatch is observed. In the end, the model combination of Oh92 with SSRT has a higher sensitivity to observation geometry changes than the model combination of IEM_B with SSRT.

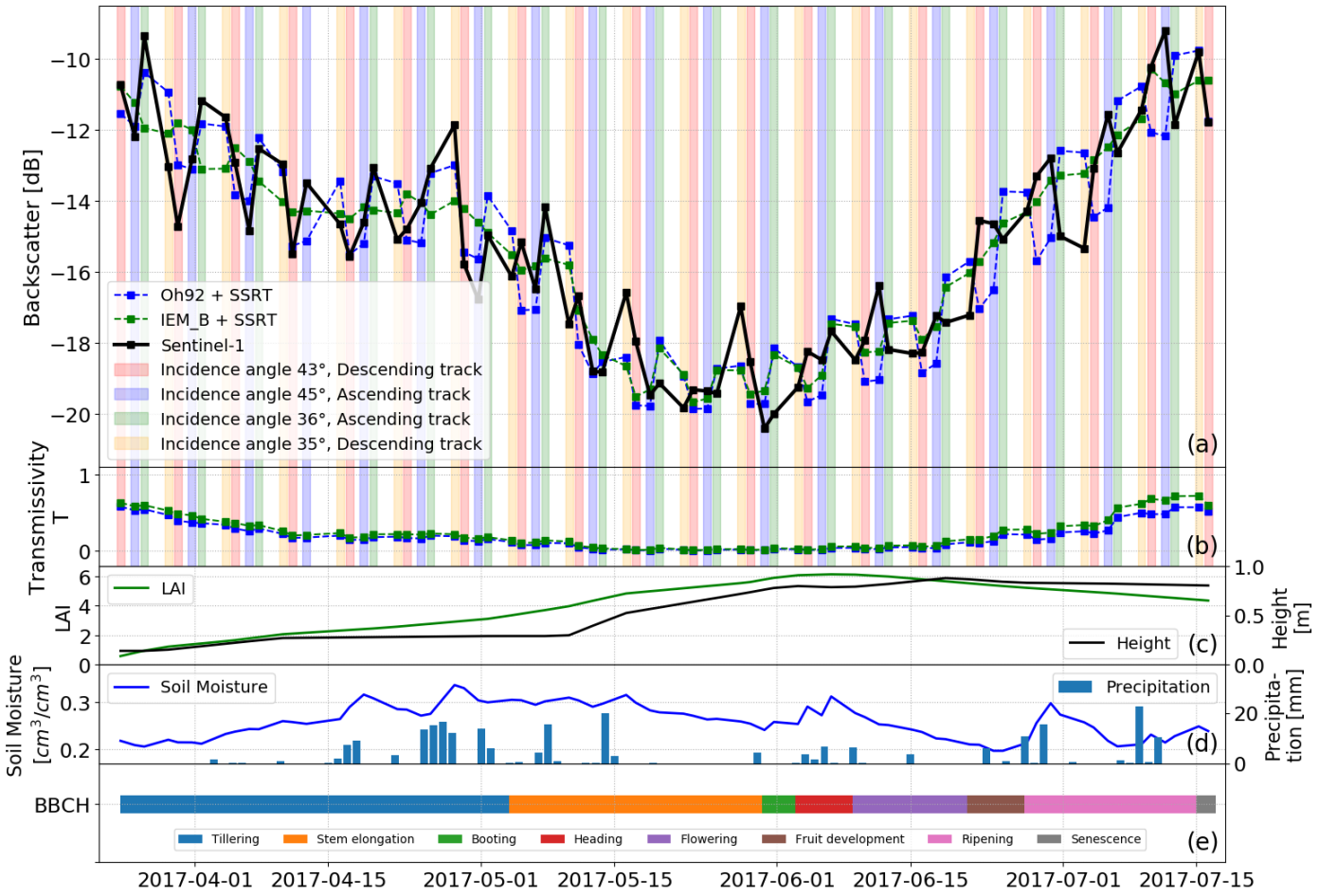

Figure 3. Sentinel-1 backscatter data for field point 508-1. Modeled backscatter results of IEM_B and Oh92 with SSRT (**a**). Different background colors (red, blue, green, and yellow) represent Sentinel-1 images with various acquisition geometries (**a**,**b**). Calibrated transmissivity T for each time step (**b**). In situ data of vegetation height and LAI (**c**). Soil moisture and precipitation measurements (**d**). Observed vegetation phenology according to the BBCH scale [57] (**e**).

4.2. Subsets of Dense Sentinel-1 Time Series

4.2.1. Analyzing Incidence Angle Variety

The data set was separated into two subsets to analyze the effect of varying incidence angles within the dense Sentinel-1 time series on the RT model results. Therefore, one subset consists only of images acquired in the same orbit direction and with the same azimuth angle ("Azi-50 m"). The azimuth angle itself is not an input parameter within the RT models, and therefore, deviations in backscatter caused by the various azimuth angles were not considered in our simple model approach. The variation in incidence angle on the other hand should cause variations in the backscatter modeled as the incidence angle is implemented as an input parameter within the RT models. The empirical model parameter $coef$ as part of the transmissivity T was calibrated for each time step using the Sentinel-1 data of each subset separately. Figure 4 illustrates the results for an azimuth angle of $-15°$ (relative to north), and Figure 5 illustrates the results for an azimuth angle of $-165°$ (relative to north). Sentinel-1 backscatter (black line), total backscatter, and the two main contributors to the total backscatter (surface and canopy part) of the models analyzed (blue and green lines) are shown in Figures 4a and 5a. For both subsets, deviations in Sentinel-1 backscatter in the range from 2 db to 3 dB between two consecutive time steps with varied incidence angles (background colors blue to green or yellow to red) are still apparent. Similar to the results shown in Figure 3, the Sentinel-1 backscatter differences of consecutive time steps observed were modeled well until the end of May. However, starting with the phenology stage of booting at the beginning of June, a trend mismatch

is observed between two consecutive time steps of Sentinel-1 and modeled data, similar to the one in Figure 3. The differences within the time series of T of Figures 4b and 5b between two consecutive time steps are similar to the modeled transmissivity illustrated in Figure 3. Since the simple RT models' sensitivity towards accurately calculating backscatter with varying incidence angles seems to be imperfect, an incidence angle normalization approach might be able to resolve or at least mitigate this issue. One of the challenges of applying incidence angle normalization approaches to the entire time series is experienced when using the analyzed Sentinel-1 data itself. The Sentinel-1 backscatter (black line within Figures 4 and 5) of consecutive time steps with different incidence angles shows higher backscatter values for steep incidence angles until the end of May and lower backscatter values for shallow incidence angles from the beginning of June. Due to this behavior, an incidence angle normalization results in either lower backscatter differences due to varying incidence angles during early phenology stages (tillering and stem elongation) and higher differences for later phenology stages (booting to senescence), or vice versa. The desired effect of the normalization in providing a smooth time series of backscatter data from wheat fields cannot be accomplished by applying one normalization approach to the entire data set. The findings indicate that a simple model approach has some deficits in simulating backscatter under various incidence angles within one time series, although the incidence angle is used as an input parameter to the models.

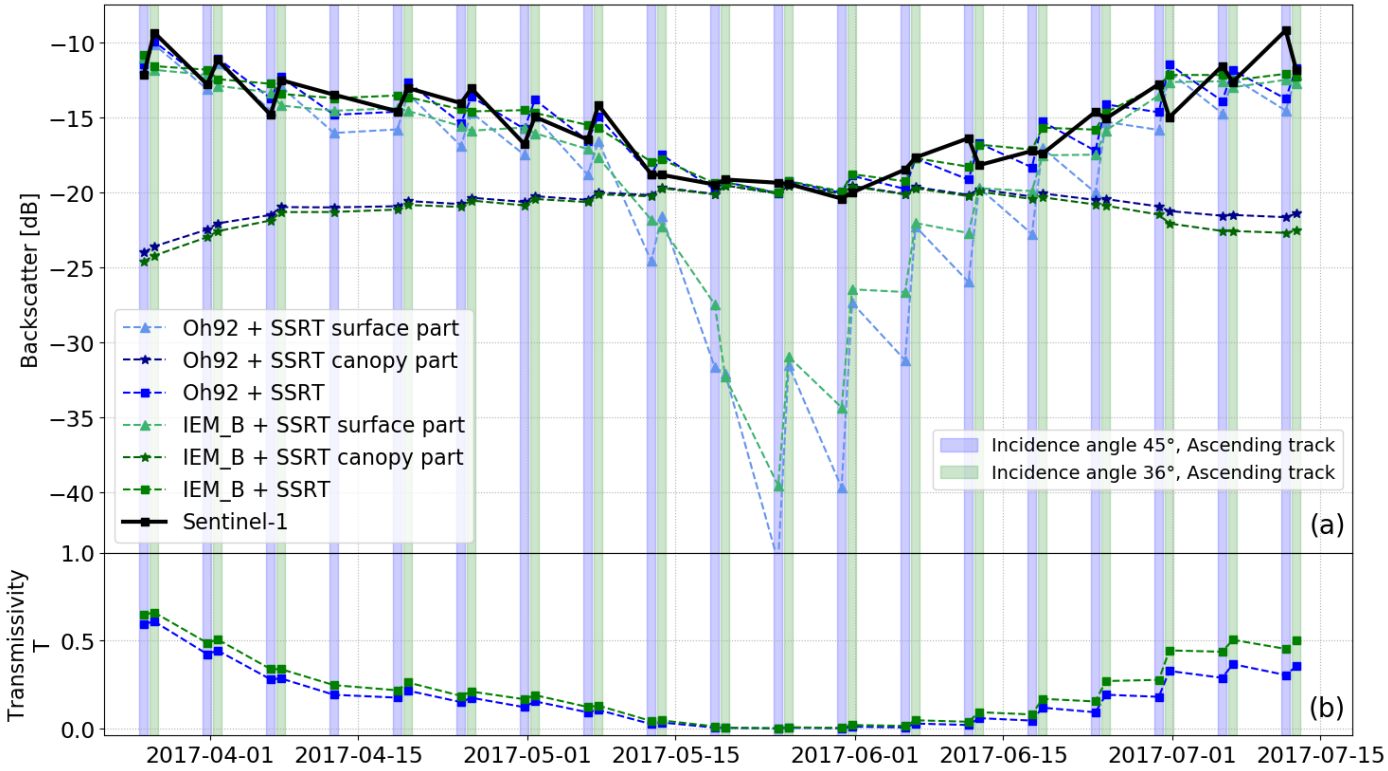

Figure 4. Sentinel-1 time series and RT model results considering images with an ascending orbit direction and an azimuth angle of −15° (relative to north) (**a**). Different background colors (red, blue, green, and yellow) represent Sentinel-1 images with various acquisition geometries (**a**,**b**). Calibrated transmissivity T (**b**).

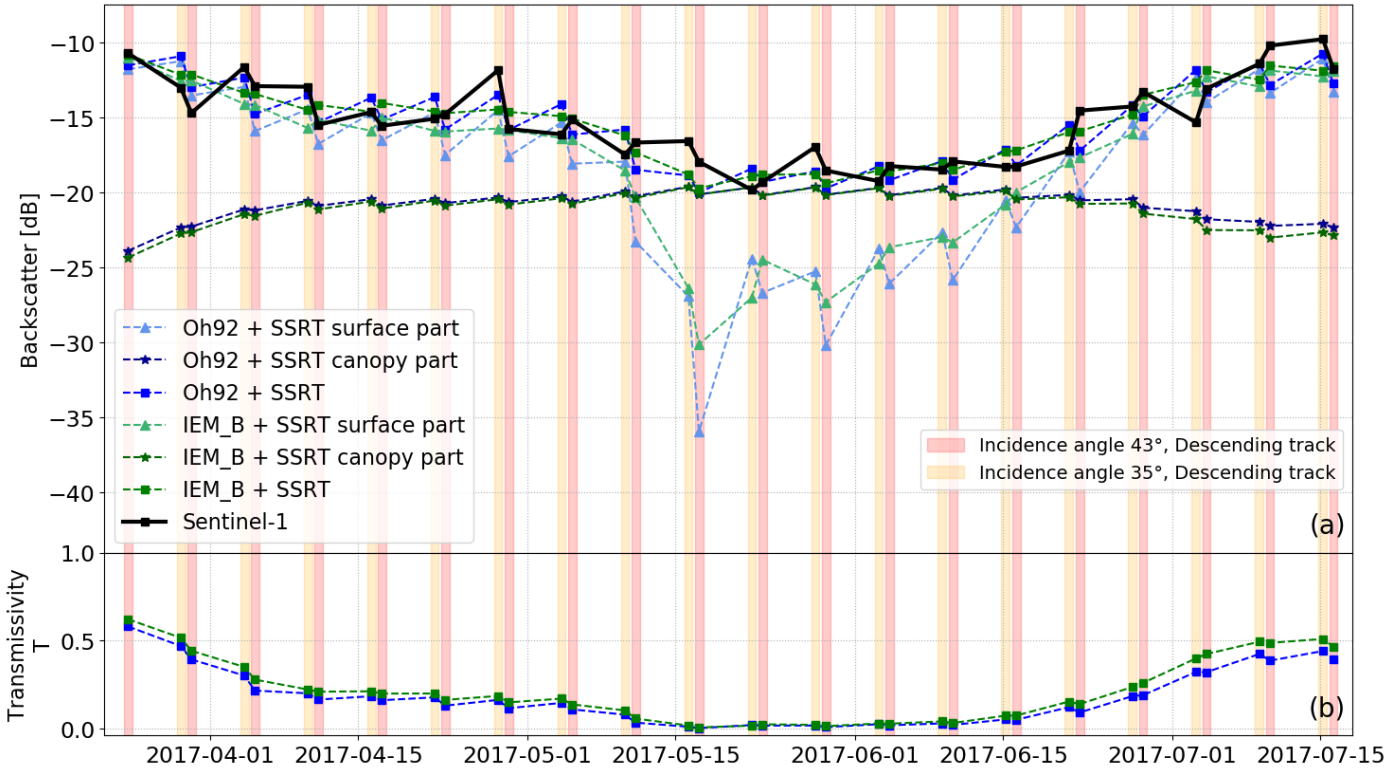

Figure 5. Sentinel-1 time series and RT model results considering images with a descending orbit direction and an azimuth angle of −165° (relative to north) (**a**). Different background colors (red, blue, green, and yellow) represent Sentinel-1 images with various acquisition geometries (**a**,**b**). Calibrated transmissivity T (**b**).

4.2.2. Analyzing Azimuth Angle Variety

The data set was split into two subsets to analyze the effect of varying azimuth angles within the dense Sentinel-1 time series and on the RT model results. Therefore, each new subset consists of acquisitions with similar incidence angles ("Inci-50 m"). Equivalent to the approach of Section 4.2.1, parameter $coef$ of the RT model combinations was calibrated using the Sentinel-1 data of each subset separately. Figure 6 shows the results for incidence angles of 35° to 36°, while Figure 7 illustrates the results for 43° to 45°. For incidence angles of 35° and 36°, higher deviations in terms of Sentinel-1 backscatter values between consecutive time steps are only visible with a significant change in soil moisture content (Figure 6c). Otherwise, distinct backscatter differences between consecutive time steps for the Sentinel-1 and RT model results are not identifiable. Additionally, the trend mismatch between the Sentinel-1 and RT model results for the phenology stages booting to senescence is not present for incidence angles 35° to 36°. The backscatter variation with incidence angles of 43° and 45° present a slightly different picture. Small discrepancies between consecutive time steps of the Sentinel-1 data are visible. However, no real trend mismatches between the backscatter values of the Sentinel-1 and RT model results are evident. For both subsets, it can be stated that, overall, the RT model predictions are in sufficient agreement with the Sentinel-1 data. Summarizing the findings, it can be stated that, although the azimuth angle is not considered as a parameter within the models, no obvious deviations between the backscatter modeled and the Sentinel-1 backscatter is observed and, thus, deviations in azimuth angles within a dense time series seems to be negligible for the model approach presented.

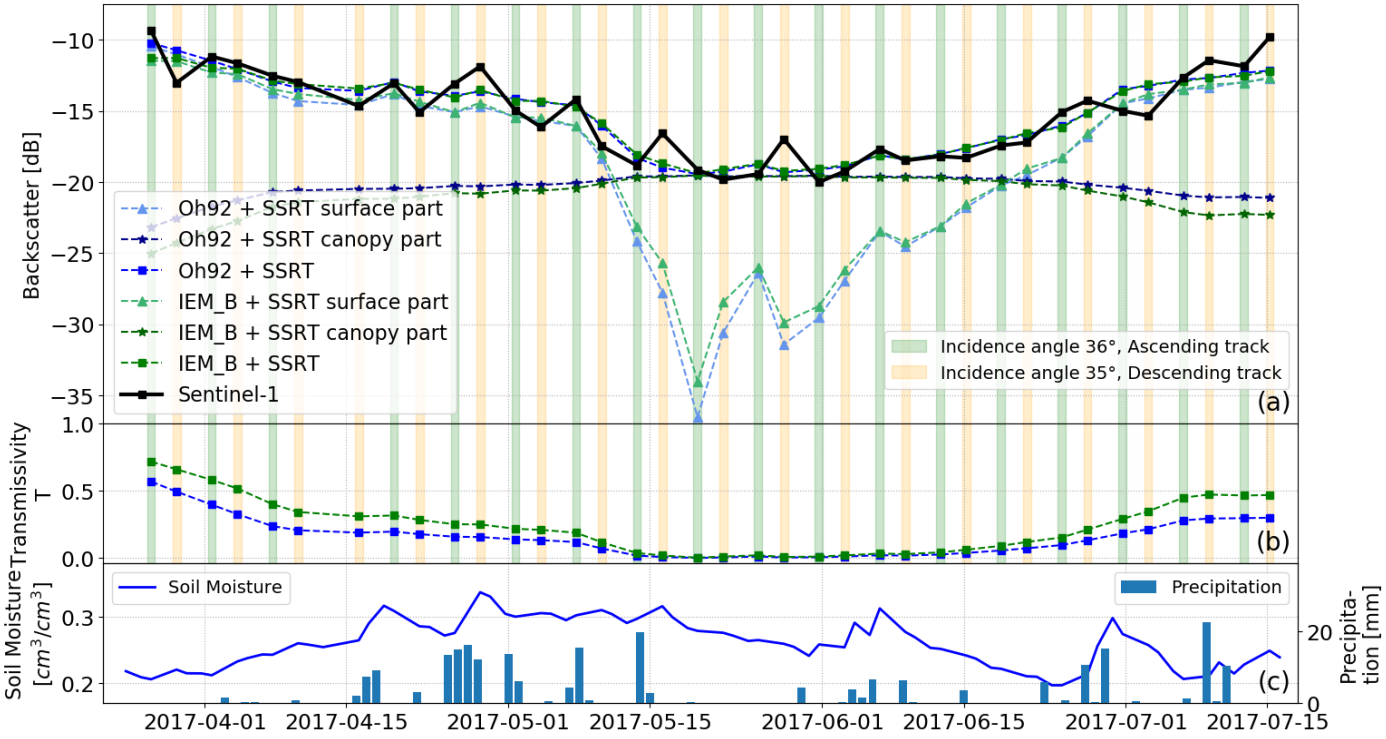

Figure 6. Sentinel-1 VV backscatter time series and RT model results for canopy and surface scattering considering images with similar incidence angles (35°, 36°) (**a**). Different background colors (red, blue, green, and yellow) represent Sentinel-1 images with various acquisition geometries (**a**,**b**). Calibrated transmissivity T (**b**). Soil moisture and precipitation measurements (**c**).

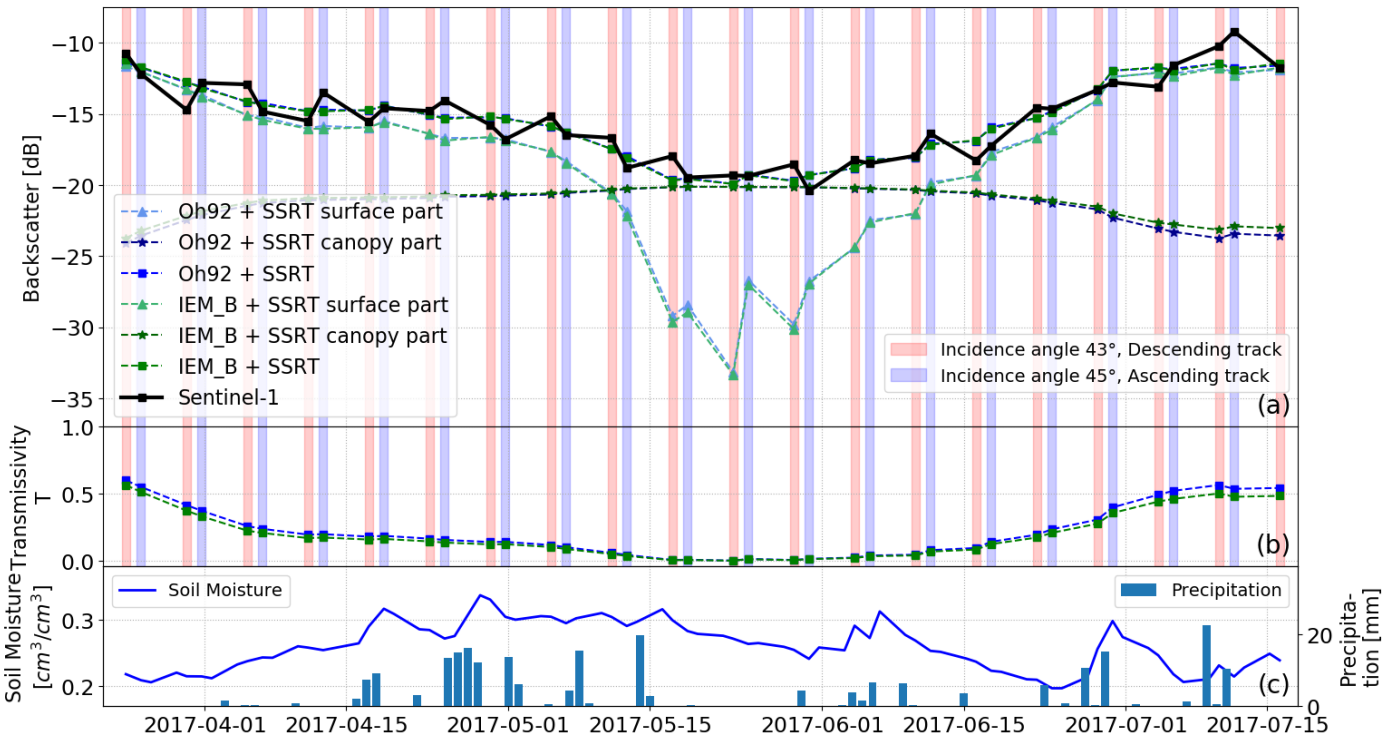

Figure 7. Sentinel-1 VV backscatter time series and RT model results for canopy and surface scattering considering images with similar incidence angles (43°, 45°) (**a**). Different background colors (red, blue, green, and yellow) represent Sentinel-1 images with various acquisition geometries (**a**,**b**). Calibrated transmissivity T (**b**). Soil moisture and precipitation measurements (**c**).

4.2.3. Separation of Dense Sentinel-1 Time Series into Mono-Incidence Data Sets

After analyzing the effects of different azimuth and incidence angles on the backscatter, the dense time series was separated into four subsets with the same orbit and, thus, the same acquisition geometry ("Sep-50 m"). The transmissivity T was calibrated by the empirical parameter $coef$ for each subset individually, and the results were reassembled into one time series afterwards. The trend mismatch between the data modeled and the Sentinel-1 data of consecutive time steps with various acquisition geometries after the beginning of June, which was detected in Figure 3, was resolved. Figure 8 shows these calibrated model results of a reassembled dense time series. Furthermore, compared to Figure 3, a sensitivity increase in the IEM_B model results in backscatter changes due to varied incidence angles being observed. The resolved trend issue and the higher incidence angle sensitivity effect result in dynamic transmissivity values by separately calibrating the empirical parameter $coef$ for varying time series subsets. Contrarily, in Figure 3, no differences of T between consecutive time steps are visible, but various values for T can be observed in Figure 8. The model combination Oh92 with SSRT shows variations in T (between Figures 3b and 8b) only after mid-July (flowering to senescence), whereas IEM_B exhibits variations during the early (tillering) and late (flowering to senescence) phenology stages. The calibrated parameter $coef$ seems to compensate for the lack of RT models in handling various acquisition scenarios in our model setup. This compensation might be forced by the model architecture and/or calibration and needs further investigation. During the phenology stages flowering to senescence, higher T values (Figure 8b) as well as higher surface model contributions (Figure 8a, triangle symbol) are observed for IEM_B and Oh92 for shallow than for steep incidence angles. Theoretically, by considering a canopy layer of 90–100 cm, the electromagnetic wave travels a farther distance through the canopy for shallow incidence angles than for steep incidence angles. Under the assumption that farther distances (shallow incidence angle) through the canopy leads to lower canopy transmissivity of the electromagnetic wave, the modeled T and the model surface component of Oh92 and IEM_B should be lower for shallow incidence angles and not the other way around. Although the model theory described cannot be seen in Figure 8, Figure 4 shows this theoretical behavior of the surface model component (Figure 4a, triangle symbol) and transmissivity (Figure 4b). However, comparing Sentinel-1 and the total modeled backscatter within Figure 4, a trend mismatch between consecutive time steps for phenology stages flowering to senescence and, therefore, differences between the Sentinel-1 and RT model total backscatter are observed.

For the results illustrated in Figure 8, no trend mismatch and thus a better fit of the data modeled and the Sentinel-1 data are observed. The reason for the discrepancy between the model theory assumed and the behavior observed might be caused by insufficient—or missing—consideration of the scattering mechanisms in the applied simplified model architecture. For a change detection analysis on scattering mechanisms and/or backscatter effects, a VV–VH dual polarimetric eigen-based (entropy (H)-scattering angle (alpha)) decomposition is performed [56]. The H-alpha results of the eigen-based decomposition are reported in Figure 9. The rows illustrate the results of consecutive time steps with various acquisition geometries (x-axis) for different vegetation stages of tillering, stem elongation, heading, and ripening (y-axis). The columns indicate the results for different incidence angles and orbit directions. During the wheat crop's tillering stage, no obvious deviations between the H-alpha results of the different acquisition geometries are recognizable. Changes in scattering effects moving from the tillering to stem elongation stages are indicated by a shift to higher H- and alpha-values. Stronger variations in the H- and alpha-values are observed for incidence angles around 35° than for 44°. The H-alpha values of the wheat fields of consecutive time steps confirm insensitivity to variations in azimuth angles of individual scenes, similar to that for backscatter. However, differences in the H- and alpha-values are observed between acquisitions with various incidence angles. Lower incidence angles of 35° reveal higher shifts in the H- and alpha-values between the tillering and stem elongation phases as well as higher H- and alpha-values

compared to incidence angles around 44°. When comparing the phenology stages stem elongation and heading, a slight decrease in H- and alpha-values is apparent. Therefore, a clear separation by incidence angle due to deviations in H- and alpha-values is possible, whereas a separation due to azimuth angles is difficult. During the ripening stage, a further decrease in H- and alpha-values is observed. Separation due to various incidence angles is possible, although not as clear as during the stem elongation or heading stages. The H- and alpha-values are similar to the values during the early vegetation stages, such as tillering. Further analysis of the different scattering mechanisms is difficult as Ji and Wu [56] found that, for VV-VH dual polarimetric eigen-based decomposition, the classification of scattering mechanisms is not as precise as for fully polarimetric ones. The various scattering mechanism classes in the H-alpha plane can have high overlap for the VV–VH dual decomposition results. Nevertheless, the change detection results show that variations in the scattering mechanism of consecutive time steps are mainly driven by the incidence angle during acquisition and not by the azimuth angle. Furthermore, similar scattering mechanisms are observed for the early (tillering) and late (ripening) vegetation stages. During the vegetation period from stem elongation to flowering stage, higher changes in scattering effects (dynamics in H- and alpha-values) are observed for steep incidence angles (35°) than for shallow incidence angles (44°). Summarizing the findings, it can be stated that, although the simplified RT models have some deficits when handling different incidence angles within one dense time series, the empirical parameter $coef$ can partly compensate for model deficiencies if each orbit is modeled separately. H-alpha decomposition is an analysis tool to explore variations in scattering mechanisms. These variations might be a possible reason for the simple model approaches having deficits in accurate backscatter modeling. H-alpha analysis indicates that, indeed, different scattering mechanism changes occur over time for different incidence angles. Moreover, variations in azimuth angles are not responsible for changes in backscatter or scattering mechanisms.

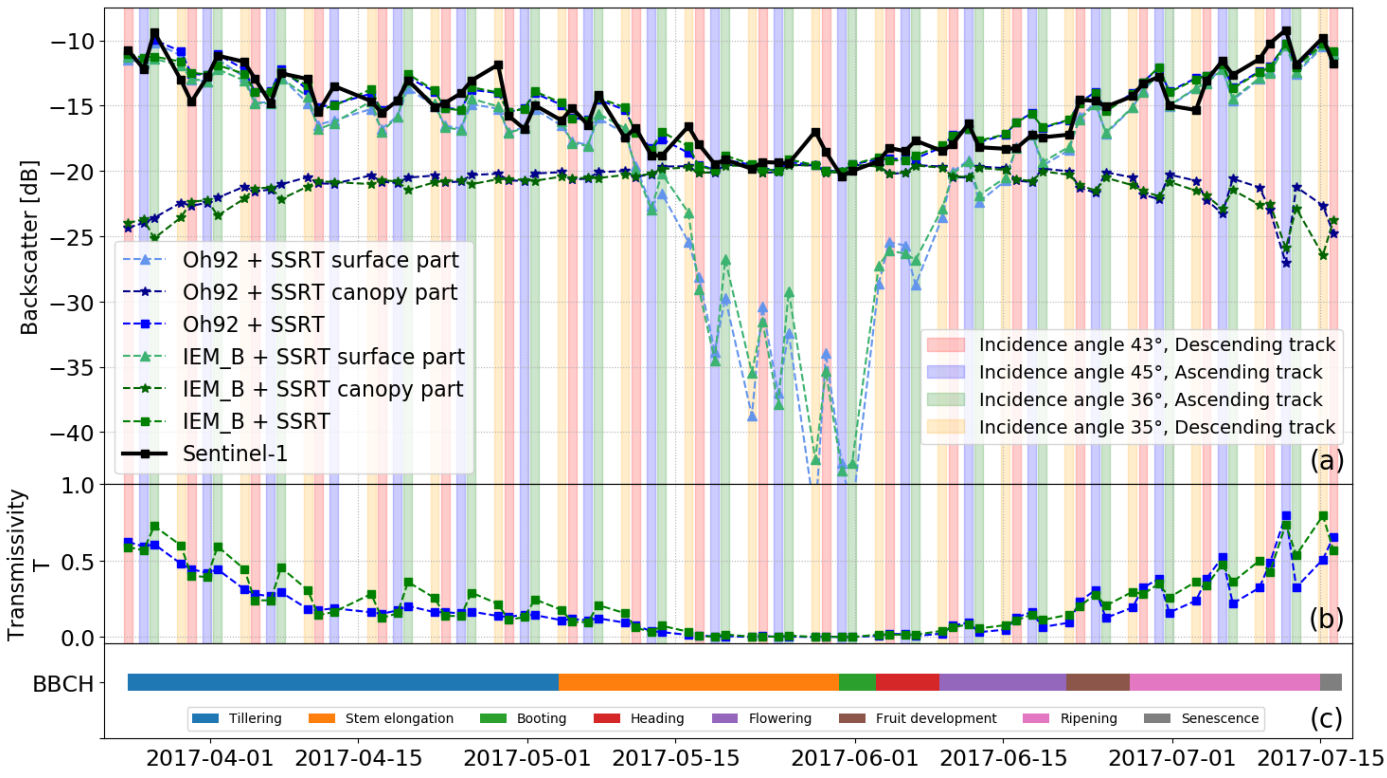

Figure 8. Joint Sentinel-1 VV backscatter time series and RT model results for canopy and surface scattering considering four mono-incidence angle data sets (**a**). Different background colors (red, blue, green, and yellow) represent Sentinel-1 images with various acquisition geometries (**a**,**b**). Calibrated transmissivity T (**b**). Observed vegetation phenology according to BBCH scale [57] (**c**).

4.3. Validation and Quantification of RT Model Results

Validation of the RT model calibration approach for the various dense time series (sub)sets was performed by a leave-one-out-cross-validation method. The mean ubRMSE of the Sentinel-1 and modeled data for all measurement field points is illustrated in Figure 10. The results are categorized by different spatial backscatter aggregations (x-axis), RT model combinations (x-axis), and (sub)sets of the dense Sentinel-1 time series used (color separation). It is expected that intra-field variances are reduced by averaging, and in this way, agreements between the model and observations might be facilitated. However, this analysis wants to quantify the model performance of the different aggregation scenarios in dB to understand the loss of precision where intra-field variance is vital. Comparing the results of Oh92 with SSRT and of IEM_B with SSRT for various Sentinel-1 data (sub)sets, greater variabilty in ubRMSE is shown for the Oh92 model combination. For both models as well as for the various data (sub)sets, spatial aggregations lead to improved ubRMSE values. The IEM_B and Oh92 results reveal improvements on the pixel to field scales by up to 0.5 dB. The best model fit in terms of ubRMSE is provided when using a time series that only considers Sentinel-1 images with incidence angles of around 35° (light green). Moreover, the ubRMSE results in a similar range to that of the best model fit are shown by using a data set with incidence angles of 43° to 45° (dark green) or if all acquisition geometry scenarios are analyzed separately (black). Overall, the IEM_B model combination reveals slightly better results than the Oh92 model combination for the different categorizations. Both model combinations analyzed by using only images with incidence angles of 35–36° (light green) compared to the entire Sentinel-1 data set (gray) improved by up to 0.3 dB. The ubRMSE of the best model fit (light green) is 1.43 dB for IEM_B and 1.64 dB for Oh92. Summarizing the results, it can be stated that the best model agreement is obtained by aggregation to the field level and by using steep incidence angles. The differences between single pixel and 30 × 30 m resolution are up to 0.2 dB, and the differences between single pixel and field scale aggregations are up to 0.5 dB.

4.4. Sensitivity to Soil Moisture Estimations over Time for the RT Model

For a comprehensive interpretation of the quantitative results illustrated in Figure 10, sensitivity analyses of the model combinations IEM_B and Oh92 with SSRT are provided in Figures 11 and 12, respectively. The figures show the deviation in estimated soil moisture with artificial variations of backscatter of 0.2 dB, 0.5 dB, and 1.0 dB. This helps in understanding how the backscatter differences modeled for different aggregation scenarios (Figure 10) result in uncertainty regarding soil moisture. It is interesting to understand that the uncertainty in soil moisture estimation differs for different phenology stages during the vegetation growing period. Uncertainty starts to increase during the stem elongation stage. This is in seen alongside an increase in vegetation height from 20 cm to 90 cm as well as an increase in LAI from 3 to 6. Due to a larger canopy layer, the transmissivity decreases, and therefore, less information about the soil and its moisture content is present within the SAR signal. During the heading stage of plants, the uncertainty begins to decrease again and it reaches its minimum during the ripening stage. Although the maximum height of the canopy is reached, the transmissivity increases and, therefore, the uncertainty of soil moisture estimations decreases. The higher transmissivity might be explained by the loss of water within the vegetation, whereby the SAR signal is less attenuated by the canopy, and therefore, the SAR signal provides more information about the soil [58–60]. Changes in incidence angles do not result in varying soil moisture uncertainties for the IEM_B model combination, whereas within the phenology stages stem elongation to fruit development, the Oh92 model combination exhibits differences in soil moisture uncertainties for varying incidence angles. For Oh92 with SSRT, a deviation in backscatter of 0.2 dB for an incidence angle change from 35° to 44° does result in an uncertainty disparity of up to 0.08 cm^3/cm^3. The results show that the uncertainties in soil moisture estimation of IEM_B and Oh92 have similar values; are highly correlated to different vegetation stages; and in the case of Oh92, are also dependent on the incidence angle.

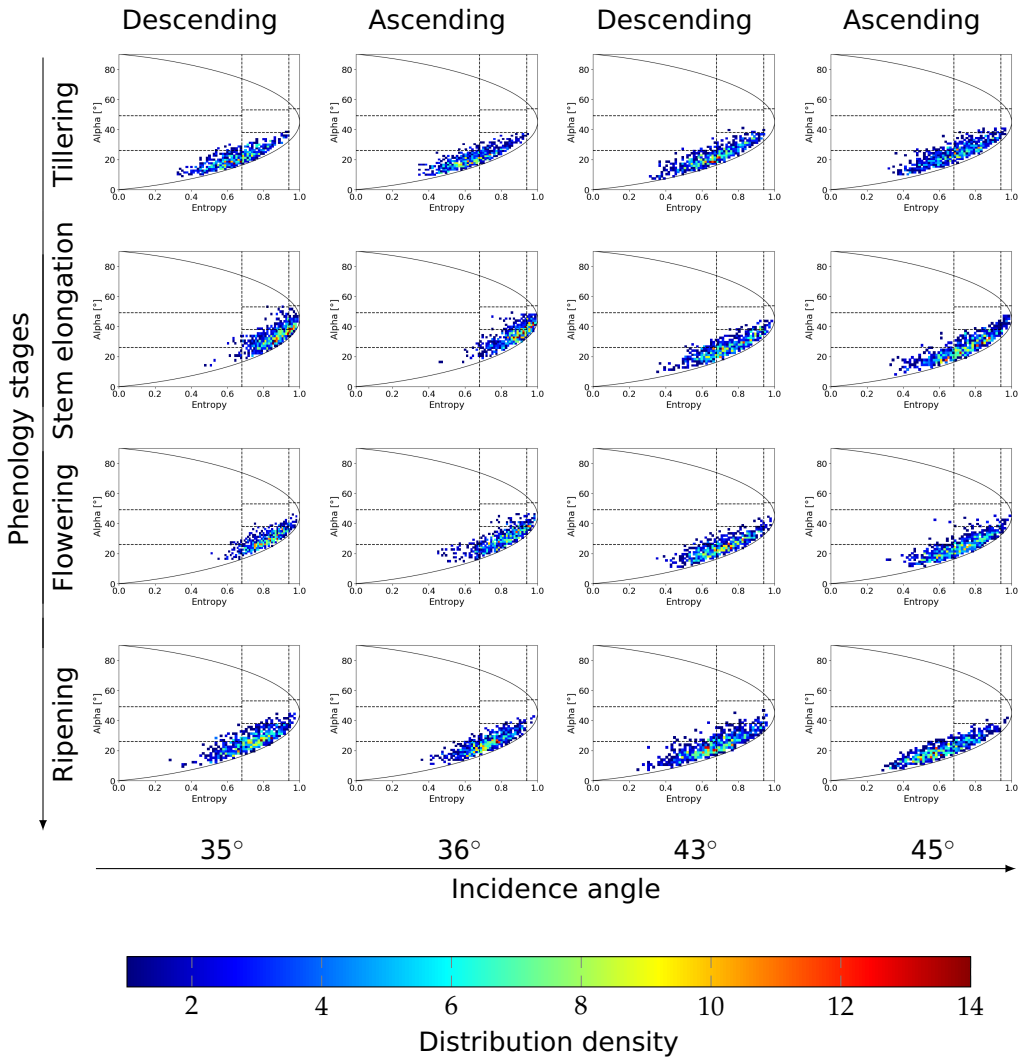

Figure 9. Polarimetric entropy to scattering alpha angle plane of dual (VV/VH) polarimetric eigen-decomposition for different incidence angles (*x*-axis) and various phenology stages (*y*-axis) of wheat field 508. Colors from blue to red symbolize the distribution density. The H-alpha plane segmentation for dual (VV/VH) polarimetric eigen-decomposition is from Ji and Wu [56].

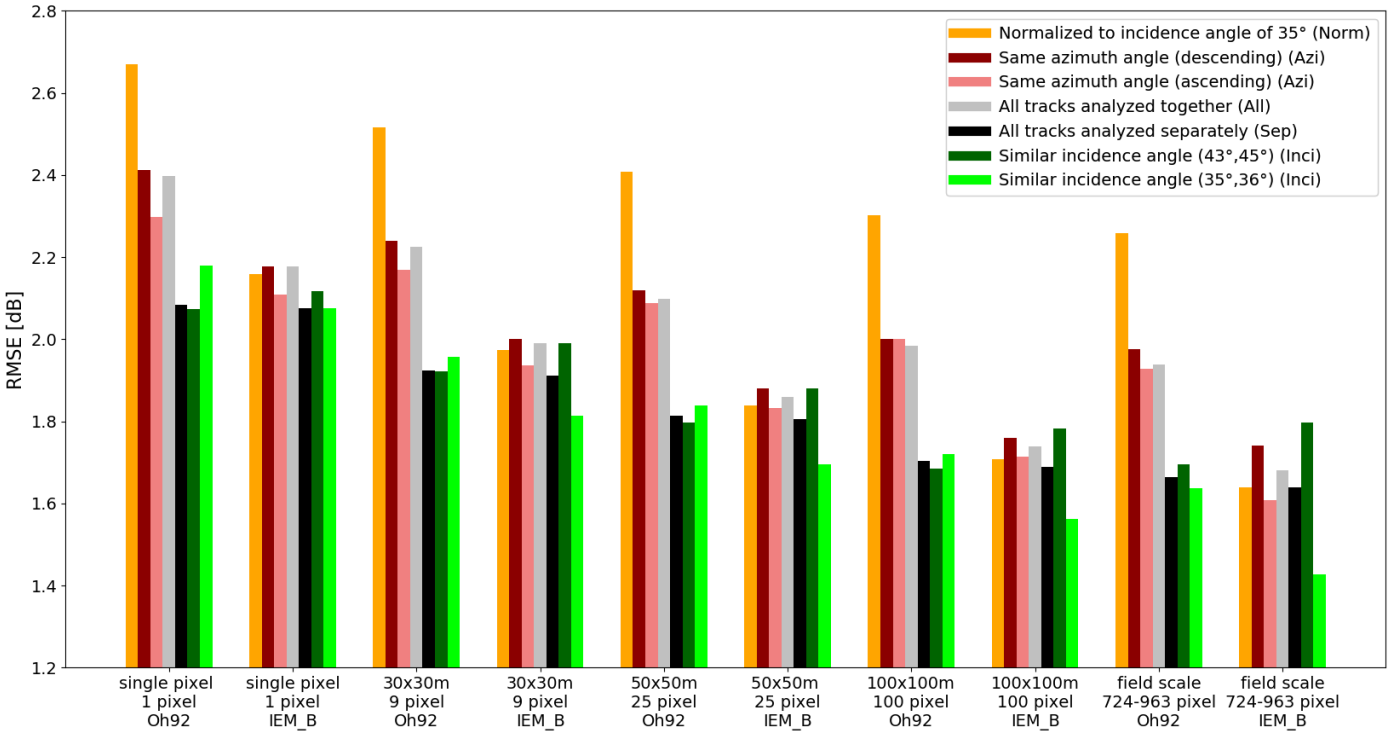

Figure 10. Validation results in terms of ubRMSE for RT models Oh92 and IEM_B with SSRT. The results are segmented in the *x* axis by different spatial aggregations (single pixel to field scale). Different colors symbolize the data (sub)sets used due to separation of incidence and azimuth angles.

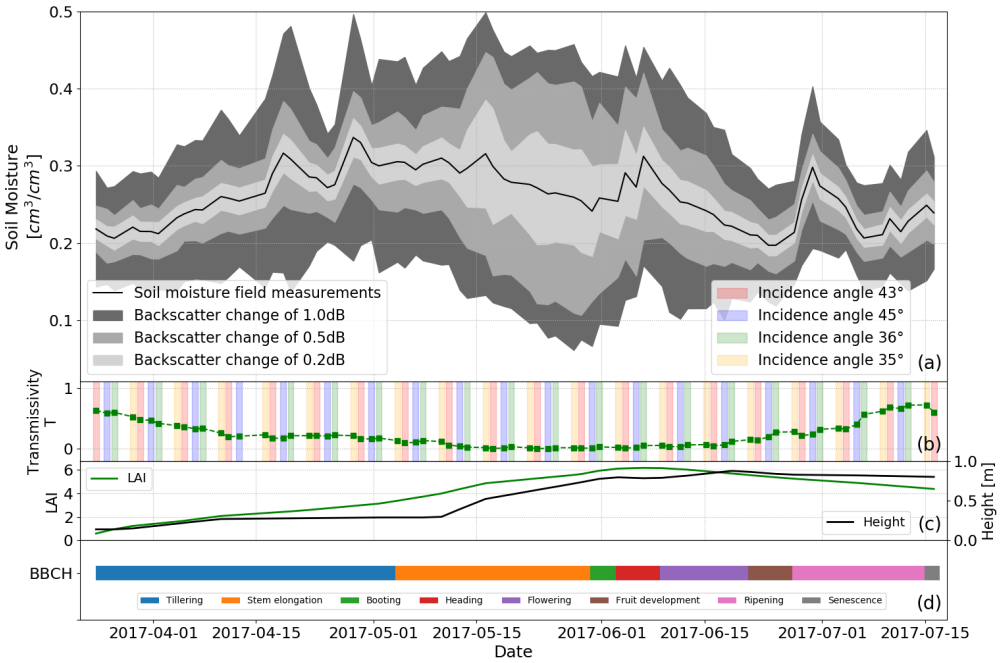

Figure 11. Sensitivity analysis of the RT model IEM_B with SSRT. Deviations in the backscatter of 0.2 dB, 0.5 dB, and 1.0 dB are correlated with soil moisture uncertainty (**a**). Different acquisition geometries (indicated by the colors red, blue, green, and yellow) of the data set used and the calibrated transmissivity for each time step (**b**). In situ data of vegetation descriptors height and LAI (**c**). Vegetation phenology observed according to the BBCH scale [57] (**d**).

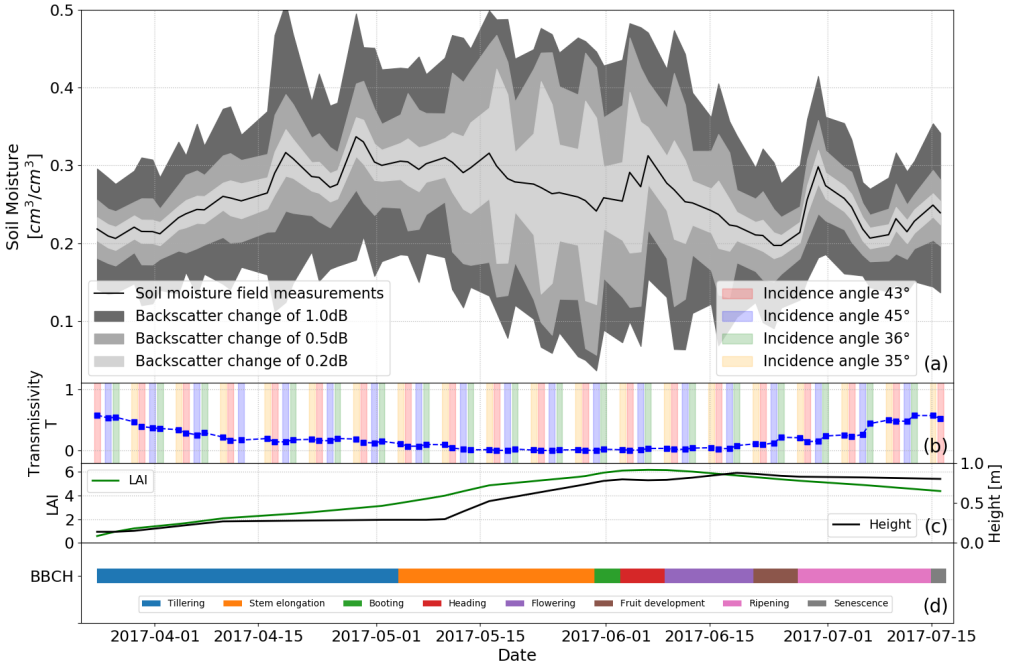

Figure 12. Sensitivity analysis of RT model Oh92 with SSRT. Deviations in the backscatter of 0.2 dB, 0.5 dB, and 1.0 dB are correlated with soil moisture uncertainty (**a**). Different acquisition geometries (indicated by the colors red, blue, green, and yellow) of the data set used and the calibrated transmissivity for each time step (**b**). In situ data of vegetations descriptors height and LAI (**c**). Vegetation phenology observed according to the BBCH scale [57] (**d**).

5. Discussion

To monitor high temporal dynamics of soil moisture, a time series with up to daily acquisitions is very useful. Currently, the Sentinel-1 satellites can provide time series with almost daily (1.5 days) acquisitions at mid-latitudes. However, due to different acquisition orbits, the images can vary in acquisition geometry and timing, which has an effect on the SAR signal. Our results show that various azimuth angles for daily consecutive acquisitions of wheat fields have only a minor impact on observed Sentinel-1 backscatter differences. However, a comparison of images with various incidence angles reveals backscatter variations in the range of up to 3 dB. Using images with similar incidence and diverse azimuth angles, backscatter variations between images of consecutive acquisition days are minimal to negligible. Lower differences in backscatter are observed for incidence angles around 35° than for 44°. A different spread of incidence angle variation in the observations (35–36° vs. 43–46°) might cause these differences in the backscatter. The lower backscatter differences between incidence angles 35–36° compared to 43–46° might be caused by the slightly higher incidence angle variation between the observations used for the different orbits. A comparison of the RT model results and Sentinel-1 backscatter observations for "All-50 m" (Figure 3) and "Azi-50 m" (Figures 4 and 5) reveal trend mismatches between the RT modeled and observed Sentinel-1 backscatter for consecutive time steps with incidence angle variations from the beginning of June until harvesting (corresponds to phenology stages from booting to senescence). When using (sub)sets with similar incidence angle and varying azimuth angles ("Inci-50 m" Figures 6 and 7), a trend mismatch between the RT model and Sentinel-1 backscatter is not found. Since the incidence angle is implemented as an input variable within the RT models applied [23,30,37,41], we expect that the RT models should be able to sufficiently consider Sentinel-1 backscatter differences due to incidence angle variations for the entire growing season. However, the trend mismatch observed in later phenological stages (booting to senescence) of the wheat fields implies that the simple model approach falls short in handling variations within a dense time series if the

canopy layer is fully developed. By calibrating the empirical parameter $coef$ for each orbit constellation separately (Figure 8), the drawbacks in precise modeling of all scattering mechanisms by simplified models (vegetation and soil) can be compensated. While more complex models might account for incidence angle variations in a more accurate way, they may be more inappropriately applied due to missing but necessary a priori/input measurements. As several studies have already found that backscatter characteristics change during or after the phenology stage of heading [60–62], we explored simple RT models by handling variations in incidence angles by performing a dual polarimetric (VV and VH) eigen-based decomposition (Figure 9). These results indicate that a change in the scattering mechanisms starts at the end of the phenology stage of stem elongation. Furthermore, they convey that varied backscatter characteristics for wheat fields might significantly depend on the incidence angle, whereas the azimuth angle seems to play a minor role. The shortcoming of simplified RT model approaches when handling various incidence angle scenarios is most likely related to inaccurate modeling of the different scattering mechanisms. As simplified models are often preferred over complex scattering models, further investigations with a larger sample of wheat fields and preferably with fully polarimetric SAR data should be carried out to verify the obtained results and to find a simple empirical or physical model solution that might be able to enhance the models by keeping their simplicity. In this context, an often-used strategy of incidence angle variations by normalizing the incidence angle [40,63–65] was ruled out. An examination of the Sentinel-1 time series of winter wheat fields observed revealed that incidence angle normalization of the entire time series are not useful due to contradicting trends between consecutive Sentinel-1 observations, variations in acquisition scenarios, and different phenology stages in the wheat growing season.

In light of exploring the possible use of Sentinel-1 data and simplified backscattering models for precision farming purposes, where sub-field variability needs to be preserved, a quantification of model-to-observation mismatch was carried out in absolute numbers (dB) for different aggregation scenarios (Figure 10). With a larger spatial aggregation, an accuracy increase in backscatter estimation (in comparison to the Sentinel-1 observations) was found that is similar to that in Pierdicca et al. [66] or Carranza et al. [64]. This was expected. However, the quantification in dB shows differences between single-pixel (SP) and 30 $\times$ 30 m (30 m) resolutions as well as single-pixel and field-scale (FS) aggregations of up to 0.2 dB and 0.5 dB, receptively. The backscatter differences found are relate to small deviations in the soil moisture estimation by 0.01 cm^3/cm^3 (SP to 30 m) and 0.02 cm^3/cm^3 (SP to FS) for the early and late vegetation stages and up to large variations of 0.13 cm^3/cm^3 (SP to 30 m) and 0.19 cm^3/cm^3 (SP to FS) for the phenology stages stem elongation to fruit development. The variations in soil moisture during the early and late vegetation stages indicate some opportunities for providing information for precision farming. However, during the phenology stages of significant vegetation growth (late stage of stem elongation to heading) the deviations in possible soil moisture estimation increase, greatly hampering precision farming applications. Since accurate soil moisture estimation highly depends on reliable information about the canopy, the fusion of optical (Sentinel-2) and microwave (Sentinel-1) time series [67–69] might provide useful phenology stage-based information in terms of LAI, NDVI, VWC, or biomass. The increase in soil moisture sensitivity of the radar signal for later vegetation stages is further related to the loss of plant water after the heading stage, which leads to a more transparent canopy layer and higher sensitivity of the radar waves to the soil surfaces [26,58,60,70]. These findings of high surface scattering during the end of the vegetation period are also supported by similar polarimetric entropy and scattering alpha values for the tillering and ripening stages (Figure 9).

6. Conclusions

Simulations of the RT model combinations (IEM_B with SSRT and Oh92 with SSRT) were compared to a dense Sentinel-1 VV backscatter time series. By considering Sentinel-1 images recorded with the available acquisition geometry, a dense time series with a mean

revisit time of 1.5 days was achieved for the winter wheat test site near Munich, Germany. Thus, different (sub)sets (separation by acquisition geometry) of the dense time series were evaluated in time and space.

Backscatter variations between individual Sentinel-1 scenes with various acquisition geometries (different orbits) were found to be mainly driven by changes in incidence angles, whereas the azimuth angle was found to be negligible. The RT models used appear incomplete regarding accurately modeling backscatter variations due to incidence angle changes for a fully developed winter wheat canopy. It was demonstrated that, when using Sentinel-1 images with the same incidence angle (mono-incidence case), the ubRMSE between the backscatter modeled and the Sentinel-1 backscatter decreases by up to 0.3 dB compared to the multi-incidence case with ubRMSEs of 1.93 dB (Oh92 with SSRT, "Sep-FS") and 1.68 db (IEM_B with SSRT, "Sep-FS"). The best fit results between the backscatter modeled and the Sentinel-1 backscatter were achieved by selecting scenes with incidence angles around 35°. Further investigations of the scattering mechanism changes by a dual polarimetric eigen-based decomposition of the VV and VH Sentinel-1 backscatter data for wheat fields showed more significant divergence during the vegetation period for steep incidence angles of 35°. During phenological stages from stem elongation to fruit development, a clear separation in terms of polarimetric entropy and scattering alpha angle values could be made between steep (35–36°) and shallow (43–45°) incidence angles. Differences between the early vegetation stages (tillering) and late vegetation stages (ripening) were marginal. It was found that the types of scattering mechanisms that appeared during the vegetation period are also dependent on the incidence angle used during acquisition. Hence, observing with a dense time series of Sentinel-1 and therefore diversity in incidence angle could mean mixing various scattering mechanisms, as observed in our study. Therefore, when modeling a dense Sentinel-1 time series using RT models, the models applied might need a certain flexibility in terms of model design to take into account potentially occurring scattering mechanisms and their weighting depending on acquisition scenarios and phenology stages.

An analysis of different spatial backscatter aggregation scenarios (single pixel to field scale) revealed improvements in the ubRMSE by up to 0.5 dB. Changes in backscatter between single-pixel and 30 × 30 m aggregation as well as single-pixel and field-scale aggregation were related to possible soil moisture uncertainties. Only small soil moisture uncertainty differences between different aggregation scenarios were shown for the early vegetation stages with a small canopy layer (tillering) and the late vegetation stages (ripening and senescence), where the winter wheat canopy should be almost transparent for C-band microwaves. Higher soil moisture uncertainties occurred for the vegetation stages stem elongation to heading. The sensitivity change is related to a canopy layer with 95 cm height by using C-band (5 cm wavelength) data. Hence, to estimate soil moisture under a changing vegetation cover (growing season of wheat), a variety of biomass, structure, and vegetation water scenarios have to be accounted for. Unfortunately, these changes in conditions are not easy to simulate electromagnetically with one scattering model or one model-combination. Hence, further research on approaches using shorter time series or RT models with limited variable parameters for calibration of the model might be promising prospects.

Simplified RT model approaches, such as that applied in this study, are well established for soil moisture estimation from active microwave (SAR) data. However, little attention is paid to differences caused by incidence angle variations between consecutive images. The implementation of the incidence angle within the RT models used can mislead one to assume that backscatter diversity due to variation in incidence angles is sufficiently accounted for. These differences lead to imprecise soil moisture estimations. Our study on the winter wheat fields of one growing season shows that the shortcomings of simplified RT model architectures used to handle time series consisting of images with varied incidence angles can be at least partly compensated for by including a calibration coefficient to individually parameterize the modeled transmissivity for the varying incidence angle

scenarios. Our simple approach of just calibrating one empirical parameter sheds light on the possibilities for adjusting model simulations for a dense time series of Sentinel-1 observations on winter wheat. Nevertheless, further investigations have to be carried out on the simple adaption of the RT models developed in terms of the applied calibration parameter. The usefulness of integrating possible the scattering mechanism changes between different phenology stages or the adaption of the approach presented to other crop types might be an interesting follow-up research topic.

Author Contributions: Conceptualization, T.W. and P.M.; methodology and data analyses, T.W., T.J., T.R., and P.M.; software, T.W. and A.L.; writing—original draft preparation, T.W.; writing—review and editing, T.W., T.J., T.R., and P.M.; resources, T.W., T.R., and P.M.; visualization, T.W., T.J., T.R., and P.M.; supervision, A.L and P.M.; project administration, A.L. and P.M.; funding acquisition, A.L. All authors have read and agreed to the published version of the manuscript.

Funding: The project leading to this application received funding from the European Union's Horizon 2020 research and innovation program under grant agreement No. 687320.

Acknowledgments: Thomas Weiß is truly thankful for the inspiration, ideas, and support that Alexander Löw (2 July 2017) provided.

Conflicts of Interest: The authors declare no conflicts of interest.

References

1. Erick, K. *Review of the Available Remote Sensing Tools, Products, Methodologies and Data to Improve Crop Production Forecasts*; FAO: Rome, Italy, 2017.
2. Torres, R.; Snoeij, P.; Davidson, M.; Bibby, D.; Lokas, S. The Sentinel-1 mission and its application capabilities. In Proceedings of the IEEE International Geoscience and Remote Sensing Symposium (IGARSS), Munich, Germany, 22–27 July 2012; pp. 1703–1706. [CrossRef]
3. Attema, E.; Snoeij, P.; Davidson, M.; Floury, N.; Levrini, G.; Rommen, B.; Rosich, B. The European GMES Sentinel-1 Radar Mission. In Proceedings of the IEEE International Geoscience and Remote Sensing Symposium (IGARSS), Boston, MA, USA, 7–11 July 2008; Volume 1, pp. I–94–I–97. [CrossRef]
4. Miranda, N.; Meadows, P.; Piantanida, R.; Recchia, A.; Small, D.; Schubert, A.; Vincent, P.; Geudtner, D.; Navas-Traver, I.; Vega, F.C. The Sentinel-1 constellation mission performance. In Proceedings of the IEEE International Geoscience and Remote Sensing Symposium (IGARSS), Fort Worth, TX, USA, 23–28 July 2017; pp. 5541–5544. [CrossRef]
5. Torres, R.; Geudtner, D.; Lokas, S.; Bibby, D.; Snoeij, P.; Traver, I.N.; Vega, F.C.; Poupaert, J.; Osborne, S. Sentinel-1 Satellite Evolution. In Proceedings of the IEEE International Geoscience and Remote Sensing Symposium (IGARSS), Valencia, Spain, 22–27 July 2018; pp. 1555–1558. [CrossRef]
6. Geudtner, D.; Torres, R.; Snoeij, P.; Davidson, M.; Rommen, B. Sentinel-1 System capabilities and applications. In Proceedings of IEEE Geoscience and Remote Sensing Symposium, Québec City, QC, Canada, 13–18 July 2014; pp. 1457–1460. [CrossRef]
7. Forgotson, C.; O'Neill, P.E.; Carrera, M.L.; Bélair, S.; Das, N.N.; Mladenova, I.E.; Bolten, J.D.; Jacobs, J.M.; Cho, E.; Escobar, V.M. How Satellite Soil Moisture Data Can Help to Monitor the Impacts of Climate Change: SMAP Case Studies. *IEEE J. Sel. Top. Appl. Earth Obs. Remote Sens.* **2020**, *13*, 1590–1596. [CrossRef]
8. Malenovský, Z.; Rott, H.; Cihlar, J.; Schaepman, M.E.; García-Santos, G.; Fernandes, R.; Berger, M. Sentinels for science: Potential of Sentinel-1, -2, and -3 missions for scientific observations of ocean, cryosphere, and land. *Remote Sens. Environ.* **2012**, *120*, 91–101. [CrossRef]
9. Veloso, A.; Mermoz, S.; Bouvet, A.; Le Toan, T.; Planells, M.; Dejoux, J.F.; Ceschia, E. Understanding the temporal behavior of crops using Sentinel-1 and Sentinel-2-like data for agricultural applications. *Remote Sens. Environ.* **2017**, *199*, 415–426. [CrossRef]
10. Van Tricht, K.; Gobin, A.; Gilliams, S.; Piccard, I. Synergistic Use of Radar Sentinel-1 and Optical Sentinel-2 Imagery for Crop Mapping: A Case Study for Belgium. *Remote Sens.* **2018**, *10*, 1642. [CrossRef]
11. Sadri, S.; Pan, M.; Wada, Y.; Vergopolan, N.; Sheffield, J.; Famiglietti, J.S.; Kerr, Y.; Wood, E. A global near-real-time soil moisture index monitor for food security using integrated SMOS and SMAP. *Remote Sens. Environ.* **2020**, *246*, 111864. [CrossRef]
12. Schlund, M.; Erasmi, S. Sentinel-1 time series data for monitoring the phenology of winter wheat. *Remote Sens. Environ.* **2020**, *246*, 111814. [CrossRef]
13. Trnka, M.; Rötter, R.P.; Ruiz-Ramos, M.; Kersebaum, K.C.; Olesen, J.E.; Žalud, Z.; Semenov, M.A. Adverse weather conditions for European wheat production will become more frequent with climate change. *Nat. Clim. Chang.* **2014**, *4*, 637–643. [CrossRef]
14. Dari, J.; Morbidelli, R.; Saltalippi, C.; Massari, C.; Brocca, L. Spatial-temporal variability of soil moisture: Addressing the monitoring at the catchment scale. *J. Hydrol.* **2019**, *570*, 436–444. [CrossRef]
15. Brocca, L.; Melone, F.; Moramarco, T.; Morbidelli, R. Spatial-temporal variability of soil moisture and its estimation across scales. *Water Resour. Res.* **2010**, *46*. [CrossRef]

16. Balenzano, A.; Mattia, F.; Satalino, G.; Davidson, M.W.J. Dense Temporal Series of C- and L-band SAR Data for Soil Moisture Retrieval Over Agricultural Crops. *IEEE J. Sel. Top. Appl. Earth Obs. Remote Sens.* **2011**, *4*, 439–450. [CrossRef]
17. Sishodia, R.P.; Ray, R.L.; Singh, S.K. Applications of Remote Sensing in Precision Agriculture: A Review. *Remote Sens.* **2020**, *12*, 3136. [CrossRef]
18. Zeri, M.; Alvalá, R.C.S.; Carneiro, R.; Cunha-Zeri, G.; Costa, J.M.; Rossato Spatafora, L.; Urbano, D.; Vall-Llossera, M.; Marengo, J. Tools for Communicating Agricultural Drought over the Brazilian Semiarid Using the Soil Moisture Index. *Water* **2018**, *10*, 1421. [CrossRef]
19. Tao, L.; Wang, G.; Chen, X.; Li, J.; Cai, Q. Estimation of soil moisture using a vegetation scattering model in wheat fields. *J. Appl. Remote Sens.* **2019**, *13*, 044503. [CrossRef]
20. Ouaadi, N.; Jarlan, L.; Ezzahar, J.; Zribi, M.; Khabba, S.; Bouras, E.; Bousbih, S.; Frison, P.L. Monitoring of wheat crops using the backscattering coefficient and the interferometric coherence derived from Sentinel-1 in semi-arid areas. *Remote Sens. Environ.* **2020**, *251*, 112050. [CrossRef]
21. Wu, S.; Ren, J.; Chen, Z.; Yang, P.; Li, H. Soil moisture estimation based on the microwave scattering mechanism during different crop phenological periods in a winter wheat-producing region. *J. Hydrol.* **2020**, *590*, 125521. [CrossRef]
22. El Hajj, M.; Baghdadi, N.; Zribi, M.; Bazzi, H. Synergic Use of Sentinel-1 and Sentinel-2 Images for Operational Soil Moisture Mapping at High Spatial Resolution over Agricultural Areas. *Remote Sens.* **2017**, *9*, 1292. [CrossRef]
23. Baghdadi, N.; El Hajj, M.; Zribi, M.; Bousbih, S. Calibration of the Water Cloud Model at C-Band for Winter Crop Fields and Grasslands. *Remote Sens.* **2017**, *9*, 969. [CrossRef]
24. Liu, Z.; Li, P.; Yang, J. Soil Moisture Retrieval and Spatiotemporal Pattern Analysis Using Sentinel-1 Data of Dahra, Senegal. *Remote Sens.* **2017**, *9*, 1197. [CrossRef]
25. Ma, C.; Li, X.; McCabe, M.F. Retrieval of High-Resolution Soil Moisture through Combination of Sentinel-1 and Sentinel-2 Data. *Remote Sens.* **2020**, *12*, 2303. [CrossRef]
26. Weiß, T.; Ramsauer, T.; Löw, A.; Marzahn, P. Evaluation of Different Radiative Transfer Models for Microwave Backscatter Estimation of Wheat Fields. *Remote Sens.* **2020**, *12*, 3037. [CrossRef]
27. Yan, W.; Yang, B.; Zhang, Y. Characterizing the C-Band Backscattering of Winter-Wheat Canopy with a Microwave Radiative Transfer Model. In Proceedings of the 7th International Conference on Agro-Geoinformatics (Agro-Geoinformatics), Hangzhou, China, 6–9 August 2018; pp. 1–6. [CrossRef]
28. Yan, W.; Zhang, Y.; Yang, T.; Liu, X. A Microwave Scattering Model for Simulating the C-Band SAR Backscatter of Wheat Canopy. *Am. J. Remote Sens.* **2019**, *7*, 13. [CrossRef]
29. Steele-Dunne, S.C.; McNairn, H.; Monsivais-Huertero, A.; Judge, J.; Liu, P.W.; Papathanassiou, K. Radar Remote Sensing of Agricultural Canopies: A Review. *IEEE J. Sel. Top. Appl. Earth Obs. Remote Sens.* **2017**, *10*, 2249–2273. [CrossRef]
30. Ulaby, F.; Long, D.; Blackwell, W.; Elachi, C.; Fung, A.; Ruf, C.; Sarabandi, K.; Zyl, J.; Zebker, H. *Microwave Radar and Radiometric Remote Sensing*; University of Michigan Press: Ann Arbor, MI, USA, 2014.
31. Ulaby, F.T.; Sarabandi, K.; McDonald, K.; Whitt, M.; Dobson, M.C. Michigan microwave canopy scattering model. *Int. J. Remote Sens.* **1990**, *11*, 1223–1253. [CrossRef]
32. Ferrazzoli, P.; Guerriero, L. Radar sensitivity to tree geometry and woody volume: A model analysis. *IEEE Trans. Geosci. Remote Sens.* **1995**, *33*, 360–371. [CrossRef]
33. Quast, R.; Wagner, W. Analytical solution for first-order scattering in bistatic radiative transfer interaction problems of layered media. *Appl. Opt.* **2016**, *55*, 5379–5386. [CrossRef]
34. Quast, R.; Albergel, C.; Calvet, J.C.; Wagner, W. A Generic First-Order Radiative Transfer Modelling Approach for the Inversion of Soil and Vegetation Parameters from Scatterometer Observations. *Remote Sens.* **2019**, *11*, 285. [CrossRef]
35. Attema, E.P.W.; Ulaby, F.T. Vegetation modeled as a water cloud. *Radio Sci.* **1978**, *13*, 357–364. [CrossRef]
36. Kweon, S.K.; Oh, Y. A Modified Water-Cloud Model With Leaf Angle Parameters for Microwave Backscattering From Agricultural Fields. *IEEE Trans. Geosci. Remote Sens.* **2015**, *53*, 2802–2809. [CrossRef]
37. de Roo, R.; Du, Y.; Ulaby, F.; Dobson, M. A semi-empirical backscattering model at L-band and C-band for a soybean canopy with soil moisture inversion. *IEEE Trans. Geosci. Remote Sens.* **2001**, *39*, 864–872. [CrossRef]
38. Prévot, L.; Champion, I.; Guyot, G. Estimating surface soil moisture and leaf area index of a wheat canopy using a dual-frequency (C and X bands) scatterometer. *Remote Sens. Environ.* **1993**, *46*, 331–339. [CrossRef]
39. Kumar, K.; Rao, H.P.S.; Arora, M.K. Study of water cloud model vegetation descriptors in estimating soil moisture in Solani catchment. *Hydrol. Process.* **2015**, *29*, 2137–2148. [CrossRef]
40. Li, J.; Wang, S. Using SAR-Derived Vegetation Descriptors in a Water Cloud Model to Improve Soil Moisture Retrieval. *Remote Sens.* **2018**, *10*, 1370. [CrossRef]
41. Oh, Y.; Sarabandi, K.; Ulaby, F. An empirical model and an inversion technique for radar scattering from bare soil surfaces. *IEEE Trans. Geosci. Remote Sens.* **1992**, *30*, 370–381. [CrossRef]
42. Oh, Y. Quantitative retrieval of soil moisture content and surface roughness from multipolarized radar observations of bare soil surfaces. *IEEE Trans. Geosci. Remote Sens.* **2004**, *42*, 596–601. [CrossRef]
43. Dubois, P.; van Zyl, J.; Engman, T. Measuring soil moisture with imaging radars. *IEEE Trans. Geosci. Remote Sens.* **1995**, *33*, 915–926. [CrossRef]

44. Fung, A.; Liu, W.; Chen, K.; Tsay, M. An Improved Iem Model for Bistatic Scattering From Rough Surfaces. *J. Electromagn. Waves Appl.* **2002**, *16*, 689–702. [CrossRef]
45. Baghdadi, N.; Abou Chaaya, J.; Zribi, M. Semiempirical Calibration of the Integral Equation Model for SAR Data in C-Band and Cross Polarization Using Radar Images and Field Measurements. *IEEE Geosci. Remote Sens. Lett.* **2011**, *8*, 14–18. [CrossRef]
46. Berger, K.; Atzberger, C.; Danner, M.; Wocher, M.; Mauser, W.; Hank, T. Modellbasierte Selektion hyperspektraler EnMAP Kanäle zur optimalen Invertierung von Strahlungstransfermodellen für landwirtschaftliche Kulturen. *PFG—J. Photogramm. Remote Sens. Geoinf. Sci.* **2018**, *86*, 263–272. [CrossRef]
47. Danner, M.; Berger, K.; Wocher, M.; Mauser, W.; Hank, T. Retrieval of biophysical crop variables from multi-angular canopy spectroscopy. *Remote Sens.* **2017**, *9*, 726. [CrossRef]
48. Danner, M.; Berger, K.; Wocher, M.; Mauser, W.; Hank, T. Fitted PROSAIL Parameterization of Leaf Inclinations, Water Content and Brown Pigment Content for Winter Wheat and Maize Canopies. *Remote Sens.* **2019**, *11*, 1150. [CrossRef]
49. Wocher, M.; Berger, K.; Danner, M.; Mauser, W.; Hank, T. Physically-based retrieval of canopy equivalent water thickness using hyperspectral data. *Remote Sens.* **2018**, *10*, 1924. [CrossRef]
50. Jiang, W.; Yu, A.; Dong, Z.; Wang, Q. Comparison and Analysis of Geometric Correction Models of Spaceborne SAR. *Sensors* **2016**, *16*, 973. [CrossRef]
51. Truckenbrodt, J.; Freemantle, T.; Williams, C.; Jones, T.; Small, D.; Dubois, C.; Thiel, C.; Rossi, C.; Syriou, A.; Giuliani, G. Towards Sentinel-1 SAR Analysis-Ready Data: A Best Practices Assessment on Preparing Backscatter Data for the Cube. *Data* **2019**, *4*, 93. [CrossRef]
52. Kellndorfer, J.; Pierce, L.; Dobson, M.; Ulaby, F. Toward consistent regional-to-global-scale vegetation characterization using orbital SAR systems. *IEEE Trans. Geosci. Remote Sens.* **1998**, *36*, 1396–1411. [CrossRef]
53. El Hajj, M.; Baghdadi, N.; Zribi, M.; Belaud, G.; Cheviron, B.; Courault, D.; Charron, F. Soil moisture retrieval over irrigated grassland using X-band SAR data. *Remote Sens. Environ.* **2016**, *176*, 202–218. [CrossRef]
54. Liu, Y.; Yang, Y.; Yue, X. Evaluation of Satellite-Based Soil Moisture Products over Four Different Continental In-Situ Measurements. *Remote Sens.* **2018**, *10*, 1161. [CrossRef]
55. Cloude, S. The dual polarisation entropy/alpha decomposition: A palsar case study. In Proceedings of the 3th International Workshop on Science and Applications of SAR Polarimetry and Polarimetric Interferometry (PolInSAR), Frascati, Italy, 22–26 January 2007.
56. Ji, K.; Wu, Y. Scattering Mechanism Extraction by a Modified Cloude-Pottier Decomposition for Dual Polarization SAR. *Remote Sens.* **2015**, *7*, 7447–7470. [CrossRef]
57. Meier, U.; Bleiholder, H.; Buhr, L.; Feller, C.; Hack, H.; Heß, M.; Lancashire, P.D.; Schnock, U.; Stauß, R.; Boom, T.v.d.; et al. The BBCH system to coding the phenological growth stages of plants—history and publications. *J. Für Kult.* **2009**, *61*, 41–52. [CrossRef]
58. He, L.; Tong, L.; Li, Y.; Chen, Y.; Tan, L.; Guo, C. Polarimetric analysis of radar backscatter from ground-based scatterometers and wheat biomass monitoring with advanced synthetic aperture radar images. *J. Appl. Remote Sens.* **2016**, *10*, 026008. [CrossRef]
59. Khabbazan, S.; Vermunt, P.; Steele-Dunne, S.; Ratering Arntz, L.; Marinetti, C.; van der Valk, D.; Iannini, L.; Molijn, R.; Westerdijk, K.; van der Sande, C. Crop Monitoring Using Sentinel-1 Data: A Case Study from The Netherlands. *Remote Sens.* **2019**, *11*, 1887. [CrossRef]
60. Mattia, F.; Le Toan, T.; Picard, G.; Posa, F.; D'Alessio, A.; Notarnicola, C.; Gatti, A.; Rinaldi, M.; Satalino, G.; Pasquariello, G. Multitemporal C-band radar measurements on wheat fields. *IEEE Trans. Geosci. Remote Sens.* **2003**, *41*, 1551–1560. [CrossRef]
61. Brown, S.C.M.; Quegan, S.; Morrison, K.; Bennett, J.C.; Cookmartin, G. High-resolution measurements of scattering in wheat canopies-implications for crop parameter retrieval. *IEEE Trans. Geosci. Remote Sens.* **2003**, *41*, 1602–1610. [CrossRef]
62. Harfenmeister, K.; Spengler, D.; Weltzien, C. Analyzing Temporal and Spatial Characteristics of Crop Parameters Using Sentinel-1 Backscatter Data. *Remote Sens.* **2019**, *11*, 1569. [CrossRef]
63. Mladenova, I.E.; Jackson, T.J.; Bindlish, R.; Hensley, S. Incidence Angle Normalization of Radar Backscatter Data. *IEEE Trans. Geosci. Remote Sens.* **2013**, *51*, 1791–1804. [CrossRef]
64. Carranza, C.; Benninga, H.j.; van der Velde, R.; van der Ploeg, M. Monitoring agricultural field trafficability using Sentinel-1. *Agric. Water Manag.* **2019**, *224*, 105698. [CrossRef]
65. Topouzelis, K.; Singha, S.; Kitsiou, D. Incidence angle normalization of Wide Swath SAR data for oceanographic applications. *Open Geosci.* **2016**, *8*. [CrossRef]
66. Pierdicca, N.; Pulvirenti, L.; Pace, G. A Prototype Software Package to Retrieve Soil Moisture From Sentinel-1 Data by Using a Bayesian Multitemporal Algorithm. *IEEE J. Sel. Top. Appl. Earth Obs. Remote Sens.* **2014**, *7*, 153–166. [CrossRef]
67. Pipia, L.; Muñoz-Marí, J.; Amin, E.; Belda, S.; Camps-Valls, G.; Verrelst, J. Fusing optical and SAR time series for LAI gap filling with multioutput Gaussian processes. *Remote Sens. Environ.* **2019**, *235*, 111452. [CrossRef]
68. Orynbaikyzy, A.; Gessner, U.; Mack, B.; Conrad, C. Crop Type Classification Using Fusion of Sentinel-1 and Sentinel-2 Data: Assessing the Impact of Feature Selection, Optical Data Availability, and Parcel Sizes on the Accuracies. *Remote Sens.* **2020**, *12*, 2779. [CrossRef]

69. Han, D.; Liu, S.; Du, Y.; Xie, X.; Fan, L.; Lei, L.; Li, Z.; Yang, H.; Yang, G. Crop Water Content of Winter Wheat Revealed with Sentinel-1 and Sentinel-2 Imagery. *Sensors* **2019**, *19*, 4013. [CrossRef] [PubMed]
70. Hajnsek, I.; Jagdhuber, T.; Schon, H.; Papathanassiou, K.P. Potential of Estimating Soil Moisture Under Vegetation Cover by Means of PolSAR. *IEEE Trans. Geosci. Remote Sens.* **2009**, *47*, 442–454. [CrossRef]